Calhoun: The NPS Institutional Archive

DSpace Repository

Theses and Dissertations | 1. Thesis and Dissertation Collection, all items

2022-12

PROOF OF CONCEPT FOR 3-D PRINTABLE GEOMETRY OF MICROFLUIDIC BENTHIC MICROBIAL FUEL CELL DEVICE (MBMFC) WITH SELF-ASSEMBLED WIRING

Kempa, James A.

Monterey, CA; Naval Postgraduate School

https://hdl.handle.net/10945/71488

This publication is a work of the U.S. Government as defined in Title 17, United States Code, Section 101. Copyright protection is not available for this work in the United States.

Downloaded from NPS Archive: Calhoun

http://www.nps.edu/library

Calhoun is the Naval Postgraduate School's public access digital repository for research materials and institutional publications created by the NPS community. Calhoun is named for Professor of Mathematics Guy K. Calhoun, NPS's first appointed -- and published -- scholarly author.

Dudley Knox Library / Naval Postgraduate School
411 Dyer Road / 1 University Circle
Monterey, California USA 93943

NAVAL POSTGRADUATE SCHOOL

MONTEREY, CALIFORNIA

THESIS

PROOF OF CONCEPT FOR 3-D PRINTABLE GEOMETRY OF MICROFLUIDIC BENTHIC MICROBIAL FUEL CELL DEVICE (MBMFC) WITH SELF-ASSEMBLED WIRING

by

James A. Kempa

December 2022

Thesis Advisor: Emil P. Kartalov
Second Reader: Dragoslav Grbovic

Approved for public release. Distribution is unlimited.

THIS PAGE INTENTIONALLY LEFT BLANK

REPORT DOCUMENTATION PAGE	*Form Approved OMB No. 0704-0188*

Public reporting burden for this collection of information is estimated to average 1 hour per response, including the time for reviewing instruction, searching existing data sources, gathering and maintaining the data needed, and completing and reviewing the collection of information. Send comments regarding this burden estimate or any other aspect of this collection of information, including suggestions for reducing this burden, to Washington headquarters Services, Directorate for Information Operations and Reports, 1215 Jefferson Davis Highway, Suite 1204, Arlington, VA 22202-4302, and to the Office of Management and Budget, Paperwork Reduction Project (0704-0188) Washington, DC, 20503.

1. AGENCY USE ONLY *(Leave blank)*	**2. REPORT DATE** December 2022	**3. REPORT TYPE AND DATES COVERED** Master's thesis

4. TITLE AND SUBTITLE PROOF OF CONCEPT FOR 3-D PRINTABLE GEOMETRY OF MICROFLUIDIC BENTHIC MICROBIAL FUEL CELL DEVICE (MBMFC) WITH SELF-ASSEMBLED WIRING	**5. FUNDING NUMBERS** RPQE8
6. AUTHOR(S) James A. Kempa	
7. PERFORMING ORGANIZATION NAME(S) AND ADDRESS(ES) Naval Postgraduate School Monterey, CA 93943-5000	**8. PERFORMING ORGANIZATION REPORT NUMBER**
9. SPONSORING / MONITORING AGENCY NAME(S) AND ADDRESS(ES) Office of Naval Research, Arlington, VA 22203	**10. SPONSORING / MONITORING AGENCY REPORT NUMBER**

11. SUPPLEMENTARY NOTES The views expressed in this thesis are those of the author and do not reflect the official policy or position of the Department of Defense or the U.S. Government.

12a. DISTRIBUTION / AVAILABILITY STATEMENT Approved for public release. Distribution is unlimited.	**12b. DISTRIBUTION CODE** A

13. ABSTRACT (maximum 200 words)

Extensive use of Unmanned Underwater Vehicles (UUVs) and remote equipment in future Naval operations leads to an energy logistics challenge for their rechargeable batteries. A solution to this challenge is a distributed network of renewable power sources detached from mainland power grids. One potential solution is Benthic Microbial Fuel Cell (BMFC) devices. BMFCs must be optimized and upscaled to produce power at relevant scales. 3-D printing is a promising manufacturing method to achieve scalable BMFC devices.

In this thesis, we devised, developed, and optimized a protocol for clearance of microfluidic channels using square cross-sections embedded within PolyJet 3-D-printed chips. The developed protocol demonstrated 75% volumetric clearance of the embedded channels. The protocol was then used to clear channels with T-shaped cross-sections, which were used to produce an experimental proof of principle for self-assembled wiring within the microchannels due to fluidic surface tension. These advancements have opened the door to embedded wiring for 3-D printed biofuel cells and other microfluidic technologies. When perfected and manufactured at scale, biofuel cells could provide a solution to the critical logistics problem of recharging UUVs and similar equipment employed in remote maritime environments, thereby making an exceptional contribution to the U.S. Navy, U.S. national security, and the related research fields.

14. SUBJECT TERMS energy, biofuel cells, renewable, scalable, 3-D printing, Unmanned Underwater Vehicles, UUV, Benthic Microbial Fuel Cell, BMFC	**15. NUMBER OF PAGES** 71
	16. PRICE CODE

17. SECURITY CLASSIFICATION OF REPORT Unclassified	**18. SECURITY CLASSIFICATION OF THIS PAGE** Unclassified	**19. SECURITY CLASSIFICATION OF ABSTRACT** Unclassified	**20. LIMITATION OF ABSTRACT** UU

NSN 7540-01-280-5500

Standard Form 298 (Rev. 2-89)
Prescribed by ANSI Std. 239-18

THIS PAGE INTENTIONALLY LEFT BLANK

Approved for public release. Distribution is unlimited.

PROOF OF CONCEPT FOR 3-D PRINTABLE GEOMETRY OF MICROFLUIDIC BENTHIC MICROBIAL FUEL CELL DEVICE (MBMFC) WITH SELF-ASSEMBLED WIRING

James A. Kempa
Lieutenant, United States Navy
BSME, Georgia Institute of Technology, 2016

Submitted in partial fulfillment of the
requirements for the degree of

MASTER OF SCIENCE IN APPLIED PHYSICS

from the

NAVAL POSTGRADUATE SCHOOL
December 2022

Approved by: Emil P. Kartalov
Advisor

Dragoslav Grbovic
Second Reader

Frank A. Narducci
Chair, Department of Physics

THIS PAGE INTENTIONALLY LEFT BLANK

ABSTRACT

Extensive use of Unmanned Underwater Vehicles (UUVs) and remote equipment in future Naval operations leads to an energy logistics challenge for their rechargeable batteries. A solution to this challenge is a distributed network of renewable power sources detached from mainland power grids. One potential solution is Benthic Microbial Fuel Cell (BMFC) devices. BMFCs must be optimized and upscaled to produce power at relevant scales. 3-D printing is a promising manufacturing method to achieve scalable BMFC devices.

In this thesis, we devised, developed, and optimized a protocol for clearance of microfluidic channels using square cross-sections embedded within PolyJet 3-D-printed chips. The developed protocol demonstrated 75% volumetric clearance of the embedded channels. The protocol was then used to clear channels with T-shaped cross-sections, which were used to produce an experimental proof of principle for self-assembled wiring within the microchannels due to fluidic surface tension. These advancements have opened the door to embedded wiring for 3-D printed biofuel cells and other microfluidic technologies. When perfected and manufactured at scale, biofuel cells could provide a solution to the critical logistics problem of recharging UUVs and similar equipment employed in remote maritime environments, thereby making an exceptional contribution to the U.S. Navy, U.S. national security, and the related research fields.

THIS PAGE INTENTIONALLY LEFT BLANK

TABLE OF CONTENTS

THIS PAGE INTENTIONALLY LEFT BLANK

LIST OF FIGURES

LIST OF TABLES

THIS PAGE INTENTIONALLY LEFT BLANK

LIST OF ACRONYMS AND ABBREVIATIONS

3-D	Three Dimensional
BMFC	Benthic Microbial Fuel Cell
CAD	Computer Aided Design
CNO	Chief of Naval Operations
DMO	Distributed Maritime Operations
LUSV	Large Unmanned Surface Vessel
MFC	Microbial Fuel Cell
MEMS	Micro Electro-Mechanical Systems
NPS	Naval Postgraduate School
PDMS	Polydimethylsiloxane
SMFC	Sediment Microbial Fuel Cell
TEA	Terminal Electron Acceptor
USV	Unmanned Surface Vessel
UUV	Unmanned Underwater Vehicle
UV	Ultraviolet

THIS PAGE INTENTIONALLY LEFT BLANK

EXECUTIVE SUMMARY

Extensive use of Unmanned Underwater Vehicles (UUVs) and remote equipment in future Naval operations leads to an energy logistics challenge for recharging batteries utilized by drones and other remote equipment. The Department of the Navy (DON) has been charged with achieving a climate ready force by building climate resilience and reducing climate threat [1]. A good solution to this challenge may be a distributed network of renewable power sources detached from mainland power grids. Benthic Microbial Fuel Cell (BMFC) technology has been demonstrated as an environmentally safe and sustainable source of energy and are a possible candidate for utilization as distributable, remote energy sources for use in the maritime environment.

Research conducted in 2019 at NPS demonstrated that microfluidic prototypes increased power output by four times compared to conventional microbial fuel cells [2]. To obtain practical and employable power cells at efficient cost, a microfluidic prototype capable of being 3-D printed and upscaled must be developed. To upscale by 3-D printing, an electron transport medium must be incorporated to act as electrical wiring within the structure. Hybrid printing is in its infancy and so direct printing of the electrical wiring medium is not an immediate solution. This thesis sought to find solutions to two challenges. The first challenge addressed was the development of a procedure for removing the sacrificial printing material from within the embedded micro-channels. The second challenge addressed was achieving proof of concept for self-assembly of wiring within the embedded micro-channels due to surface tension effects.

To solve the first problem, in this thesis, we devised, developed, and optimized a protocol for clearance of microfluidic channels featuring square cross-sections embedded within PolyJet 3-D-printed chips. The protocol developed in this research demonstrated about 75% volumetric clearance of the embedded channels. This research saw success in creating square cross-section channels featuring widths of ~200μm.

The second problem addressed by this thesis focused on effectual development and proof of concept of self-assembly of internal wiring based on fluidic surface tension within

the microfluidic channels. Self-assembly of wiring is based on flowing a hydrophobic conductive liquid in microchannels with T-shaped based cross-sections, then flushing with water. Surface tension would keep the conductive liquid inside the narrow sections, while the wide section is cleared for use with bacteria and biomass. The result will be a self-assembled 3-D network of fuel cells and associated internal wiring.

To solve the second problem the clearing protocol developed in the first part of this thesis' research was used to clear channels with T-shape based cross-sections. These channels were then used to produce an experimental proof of principle for the T-channel and fluidic surface tension method of self-assembly of fluids inside embedded channels. The proof of principal experiments used a color dyed oil to represent the wiring medium and fresh water to represent the bacterial slurry. When the channels were viewed from above, the desired effect appeared with dark colored outer edges, where the "T" flanges are located, and a clear central portion filled with the water.

These advancements have opened the door to embedded wiring for 3-D printed biofuel cells, as well as any other microfluidic technology that can benefit from 3-D printing. As such, this thesis has made a major contribution to the related fields. When perfected and manufactured, biofuel cells could provide a solution to the critical logistics problem of recharging UUVs and similar equipment employed in remote maritime environments, thereby making an exceptional contribution to the U.S. Navy and U.S. national security.

References

[1] "Department of the Navy Climate Action 2030 220531.pdf." Department of the Navy, Office of the Assistant Secretary of the Navy for Energy, Installations, and Environment, May 2022. Accessed: Jul. 12, 2022. [Online]. Available: https://www.navy.mil/Portals/1/Documents/Department%20of%20the%20Navy%20Climate%20Action%202030%20220531.pdf?ver=3Q7ynB4Z0qUzlFg_2uKnYw%3d%3d&timestamp=1654016322287

[2] T. D. Nguyen, "Output power optimization of microbial fuel cells by scalable microfluidic devices," Monterey, CA; Naval Postgraduate School, 2019.

ACKNOWLEDGMENTS

I would like to thank the U.S. Navy for the opportunity to pursue this degree.

I would like to thank ONR, Dr Laura Kienker (N0001420WX01371, N0001421WX01680), and Dr Kristy Hentchel (N0001422WX01299) for their continued support and funding of this research.

I would like to thank Dr. Emil Kartalov for his mentorship, guidance, and support.

I would like to thank Captain (Ret) John Hammerer for his mentorship, and support. I would like to thank Commander Richard Arledge for his mentorship and guidance.

I would like to thank Dr. Dragoslav Grbovic for his guidance, and support.

I would like to thank Jeffrey Catterlin for his efforts in support of this research.

I would like to thank Terak Hornik for his efforts in support of this research.

I would like to thank Marcus A. Worsley for his efforts in support of this research.

I would like to thank Troy Ansell for his efforts in support of this research.

Finally, I would like to thank my spouse, family, and friends for their love and support.

THIS PAGE INTENTIONALLY LEFT BLANK

I. INTRODUCTION

> The nation has committed to achieve net-zero emissions economy-wide by 2050.
>
> —Department of the Navy Climate Action 2030

The Department of the Navy (DON) has been charged with achieving a climate ready force by building climate resilience and reducing climate threat [1]. The DON has committed to reducing one million cars' worth of carbon dioxide equivalent emissions by 2027 through land management, micro electrical-grids, and similar technologies [1]. Sustainable, clean energy is an ever-increasing concern as societal demand for technologies and modernization grow. Petroleum, natural gas, and coal are the dominant fuel sources across the globe for providing the energy demanded by societies; however, there are serious concerns surrounding the burning of fossil fuels and the associated emissions released [2], [3]. Additionally, the stability of supply lines of these fuels is heavily linked to the geopolitical and economic environment. Both the Chief of Naval Operations' (CNO) NAVPLAN 2021 [4] and the Report to Congress on the Annual Long-Range Plan for the Construction of Naval Vessels [5] express significant uptick in leveraging unmanned technologies including Unmanned Underwater Vehicles (UUVs) and Unmanned Surface Vessels (USVs) with projections for the number of UUVs and USVs collectively ranging between 77 and 140 vessels [5]. In addition to supporting the Nation's clean energy initiatives, microbial fuel cell (MFC) technologies could directly support the CNO's NAVPLAN 2021 and NAVPLAN 2022 by supporting the Distributed Maritime Operations (DMO) concept, "Integrated All Domain Naval Power" and operations in remote and contested environments [4], [6]. This research seeks to build on the knowledge gained from the 2019 NPS research with focus on microfluidic architecture and microelectrode configuration. This work sought to create a 3-D printable microbial fuel cell architecture capable of self-assembly of internal wiring that enables scalability at an economic advantage.

A. MICROBIAL FUEL CELLS

Microbial fuel cells seek to harness electricity from chemical reactions between bacteria and biomass [3]. Bacteria in a biomass act as an anode and interact with an oxygen rich environment that acts as a cathode [3]. The bacteria oxidize material in the biomass which releases electrons [3]. Some of the released electrons are used by the bacterial cells, but some electrons are available to be harnessed [3]. The amount of energy generated from the oxidization process and available for harnessing depends on many factors including the materials involved, the geometry of the fuel cell, and the types of electrodes or Terminal Electron Acceptors (TEA) utilized [3]. The process was first described early in the twentieth century with the first functional prototype of a Benthic Microbial Fuel Cell (BMFC) being demonstrated in the early 2000s [7].

A few of the existing MFC architectures include: single and double-chamber air-cathode, flat-plate, single chamber with graphite-metal cathode, and aqueous cathode with dissolved oxygen [3]. These architectures are not able to be manufactured in large quantities quickly nor are they easily arrayed to produce larger quantities of power. Developing a scalable MFC architecture is a primary motivation and goal for this research.

B. NAVAL APPLICATIONS

The Office of Naval Research, an entity mandated by Congress to conduct "specialized and imaginative research," envisions the future of naval forces as "the small, the agile, and the many" [8]. Manned or unmanned underwater vehicles are envisioned to utilize distributed networks for communications as illustrated in Figure 1. This concept could be expanded to utilize distributed networks of microbial fuel cell stations for charging batteries used for propulsion, sensors, and habitability while supporting sustained operations in remote environments.

One conceptualization for employment of these BMFC stations is the devices being pre-fueled, delivered for operation and then recovered. In this concept, delivery could be achieved by a variety of platforms including ships, submarines, and aircraft to the operating areas where they could support energy needs for a relatively short, ~weeks, but critical amount of time. An alternative concept could be BMFCs delivered in the same manner but

with the capability to refuel themselves by periodically taking in fresh biomass from the surrounding environment. The self-refueling capability is a technology yet to be deeply explored for this application but could support energy needs for significantly increased durations of time.

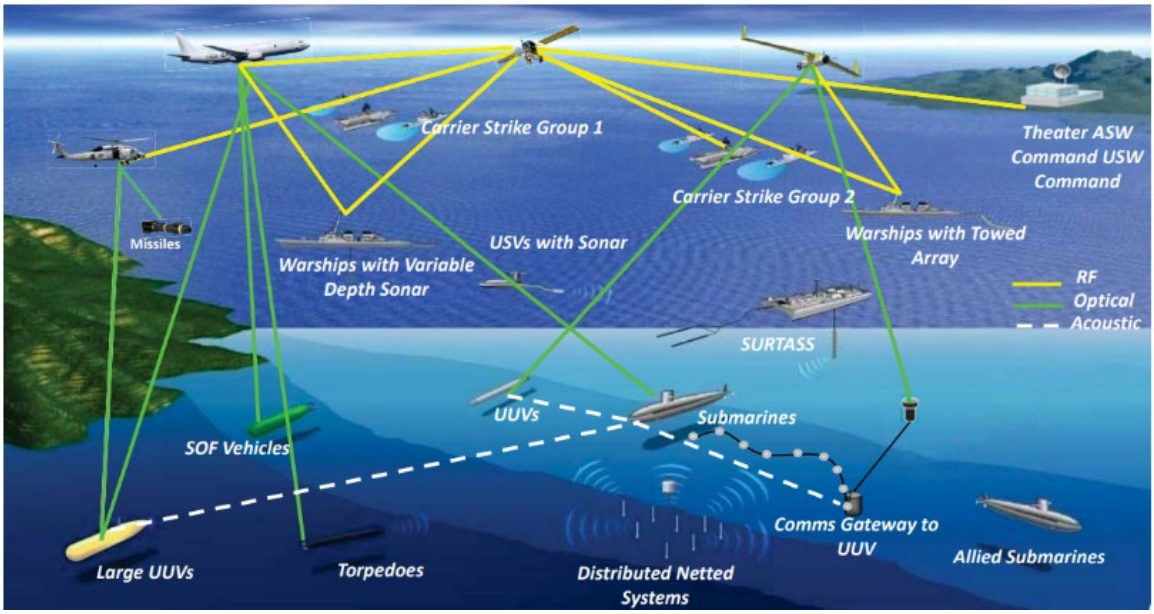

Figure 1. Distributed Communications Visualization. Source: Filipoff (2018).

Beyond military applications, any marine vessels operating with battery-powered electric motors could use distributed microbial fuel cell supported stations for charging. In this capacity, these stations could be set up to support charging from anchorages to service a wide variety of vessels including private, commercial, or military. This concept can be thought of as analogous to electric vehicle charging stations that are not connected to a land-based power grid.

C. CURRENT MFC TECHNOLOGY

Many MFC designs contain two chambers, one for the anode and the other for the cathode, separated by a Cation Exchange Membrane (CEM) to facilitate the exchange of ions [3]. Several types of MFC architectures have been developed and tested with power

densities ranging from 3 mW/m^2 to 1540 mW/m^2 [3], [9]. These power density values are small compared to more conventional electricity generation methods which yield orders of magnitude more wattage per area. These low power densities have inspired research into optimizing the design of MFCs to increase the power densities as well as exploration of applications in remote and unique environments where existing energy sources are unavailable or impractical.

Applications for MFC technologies is an active area of exploration and is likely to expand as the technology is improved. One promising application of MFC technology for renewable energy generation is in wastewater treatment facilities where energy can be extracted from the natural decay of wastes that traditionally have only required energy input to create a useable product [3]. Another application of this technology can be found in the marine environment. The seabed, known as the benthic zone, containing biomass and bacteria, can host an anode, whereas the seawater above can host a cathode [3]. The sediment layer between the seabed and the seawater above facilitates oxygen diffusion from the seawater eliminating the need for an ion exchange membrane [7]. This configuration has proven to yield electricity generation sufficient to support small energy needs such as aquatic sensor and device charging [3], [7]. This configuration is referred to as a Sediment Microbial Fuel Cell (SMFC) or BMFC [3].

In 2019, research trials conducted at the Naval Postgraduate School (NPS) demonstrated average output power densities of ~120 mW/m^2 [9]. The trials that lasted ~30 days and recorded a peak measurement at ~160 mW/m^2 [9]. These results were a notable improvement from previous results at the time of ~3-30 mW/m^2 [9]. The 2019 NPS research developed a microfluidic, polydimethylsiloxane (PDMS) chip shown in Figure 2. The chip posed a microchannel width of ~100-microns with a ceiling height of ~90-microns and was used as a test bed for investigating other parametric factors influencing output power. PDMS was chosen as it is an organically inert, silicon-based material already widely in use for elastomeric devices used in various biotechnology

applications [9]. The dimensions were chosen to balance volumetric capacity of the bacterial slurry with proximity to the electrodes [9].

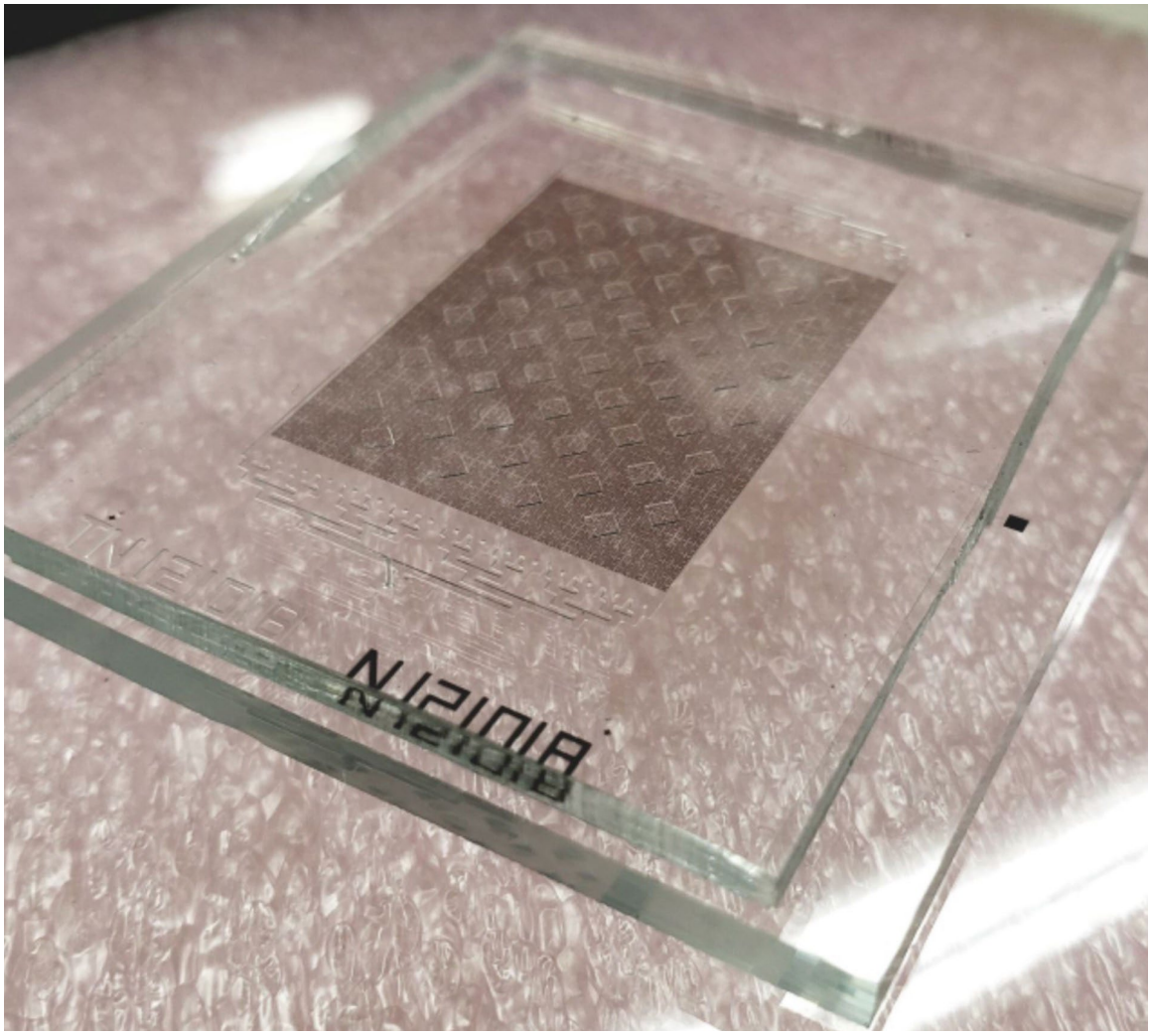

Figure 2. "Assembled Microfluidic MFC Chip." Source: Nguyen (2019).

This MFC was composed of two components, a micro-electrode wiring matrix base, Figure 3, with the PDMS Dome Template, Figure 4, applied on top [9]. The wiring matrix base was constructed utilizing Micro Electro-Mechanical Systems (MEMS) fabrication methods including photolithography and wet etching [9].

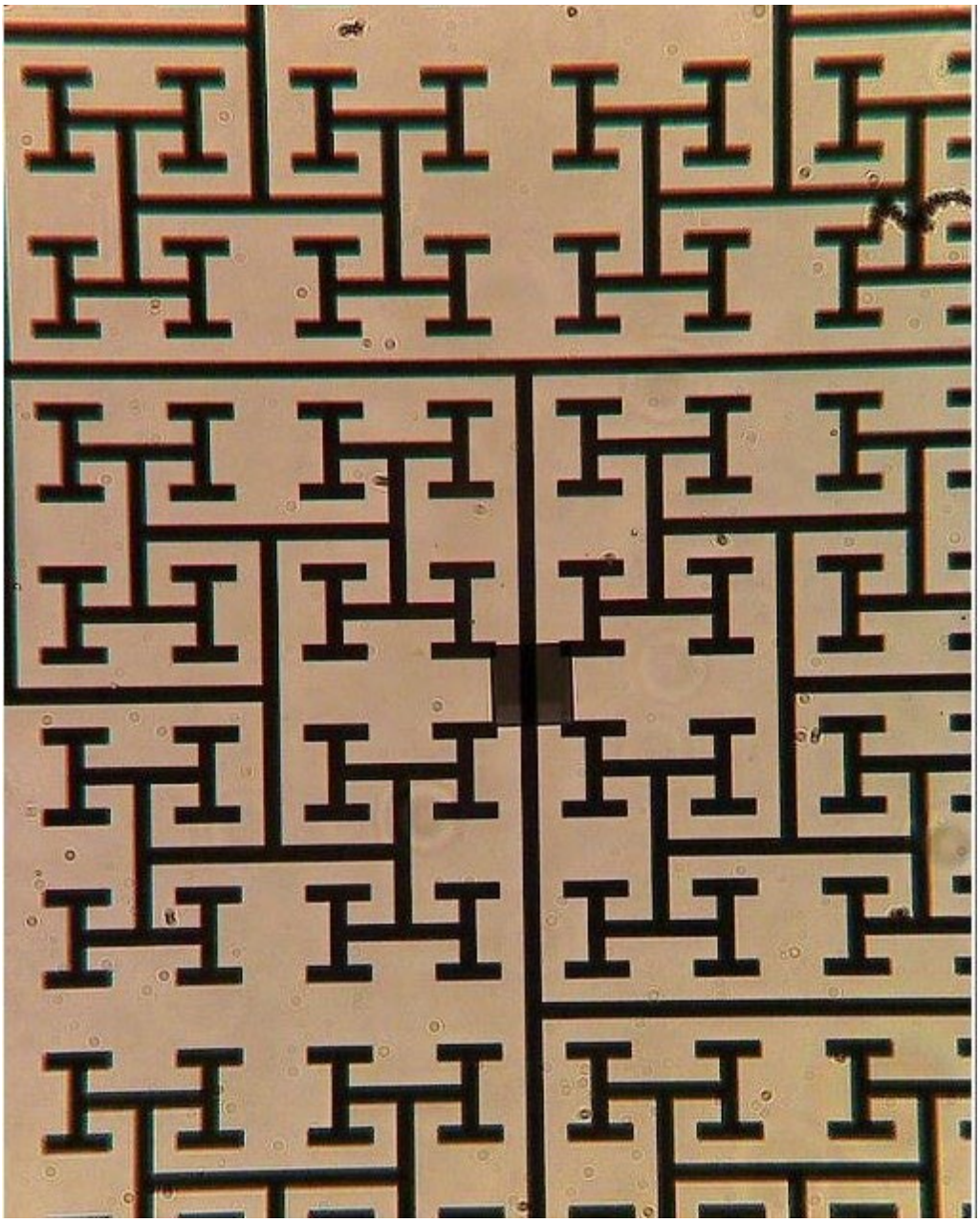

Figure 3. Chrome on Glass Electrode Wiring Matrix. Source: Nguyen (2019).

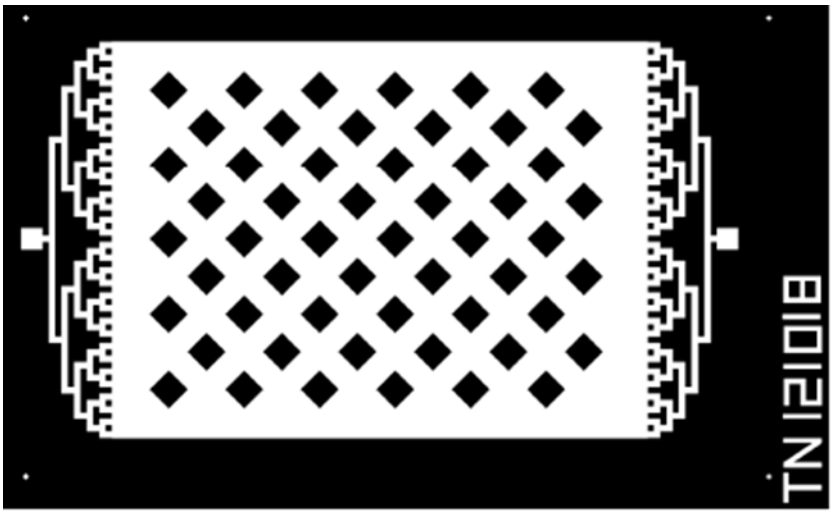

Figure 4. "PDMS Dome Template." Source: Nguyen (2019).

In addition to achieving increased power generation per unit area, the research concluded that factors including microelectrode configuration, microfluidic architecture, cellular concentration, and biomass media content were all areas where additional research and optimization could yield further increases in output power densities [9]. A notable limitation of the PDMS dome combined with the chrome-on-glass base is that this design is expensive and time consuming to create. Additionally, this design is not easily scaled up to yield higher overall device power outputs. Additive manufacturing (3-D printing) is an alternative method of production that may help to overcome these limitations.

D. MICROBIAL FUEL CELLS AND 3-D PRINTING

A challenge that researchers continue to face with MFC advancement is scalability and cost in manufacturing of the reactor architectures. The small energy densities presented by MFCs require that relatively large areas must be utilized to harness larger quantities of energy required by many applications. Multiple-component manufacturing and assembly can be costly in terms of time and monetary resources. 3-D printing is an additive manufacturing process by which layers of material are deposited successively until the final structure is complete. This method of production produces less waste compared to subtractive manufacturing process which achieves the desired structure by removing material from a larger block of material.

3-D printing allows for the rapid creation of three-dimensional structures with internal aspects from computer-generated models. The sizes and complexities achievable through 3-D printing are highly dependent upon the specific printing equipment being utilized but generally range from details of ~10 microns to structures the size of small vehicles or homes; these are the extremes, with most printers capable of print volumes less than 0.05 cubic meters. The range of materials available for use in 3-D printing has grown rapidly spanning various types of plastics to metals. Some 3-D printers are even capable of hybrid printing, where multiple materials are printed during a single run. Hybrid printing allows for the creation of complex geometries including internal structures and voids. To create internal voids, sacrificial material is deposited where the void is desired during the print and then is removed after the print is complete in post processing procedures.

3-D printing technology yields the possibility of scalable MFC production by creating arrays of 3-D printed components to overcome lower power densities at modest financial cost and time investments. To illustrate the power obtainable from an array of MFCs, here is a simple example. Using a 1 square meter footprint, a representative value of $100 mW/m^2$ for the power per unit area, and a 100-micron channel width per MFC unit, the power available from a scaled array of MFCs can be calculated by Equation 1.1

$$Power = \frac{100 mW}{m^2} \times 1 m^2 \times \frac{1 m}{100 \mu m} = 0.1 W \times \frac{1000 mm}{0.1 mm} = 1 kW \tag{1.1}$$

The following chapters present the experimental methodology, results, and conclusions from this research.

II. EXPERIMENTAL METHODOLOGY AND MATERIALS

This chapter presents the design conceptualizations, modeling and fabrication methods, and testing and evaluation procedures utilized in this research. This research involved two major components. The first explored chips embedded with square cross-section channels with a focus on determining the dimensional limits of the printer and developing a clearing procedure for removing sacrificial material from the channels after printing. Secondly, the clearance procedure was performed on chips embedded with "T" based cross-section channels. These "T" shaped cross-section channels were used to demonstrate proof of principle for self-assembly of internal wiring.

A. DESIGN CONCEPTUALIZATION

Microfluidic devices are operated in low Reynolds Number regimes. The Reynolds Number is the ratio of inertial forces compared to viscous forces and can be represented by

$$\mathrm{Re} = \frac{\rho V L}{\mu} \tag{2.1}$$

where ρ is the density of the fluid, V is the local velocity of the fluid, L is a characteristic length, and μ, is the dynamic viscosity. In circumstances where the Reynold's Number is low, viscous forces dominate inertial forces and fluid flow is laminar; this is conducive for the bacteria and supports fluid layer separation. To simplify manufacturing and leverage the advantages 3-D printing offers, an architecture concept capable of supporting both the bacterial slurry and self-assembled electrode wiring was developed as shown in Figure 5. The basic architecture is a channel featuring a "T" shaped cross-section (A & B) where the horizontal cavity, highlighted blue in (C), will house the bacterial slurry and the vertical stem, highlighted in yellow in (D), will host the electrode wiring.

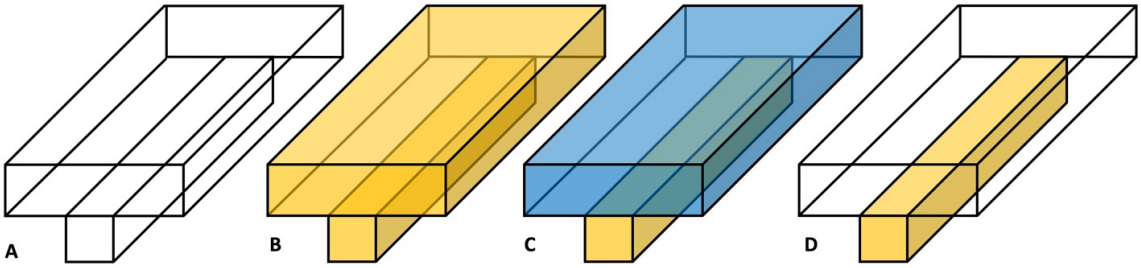

"T" Channel architecture concept. The blue section in (C) is intended to house the bacterial slurry and the smaller yellow channel below is intended to host the electron capture and transport medium acting as wiring.

Figure 5. "T" Channel Architecture Design Concept

From this design architecture, two fabrication concepts emerged to achieve the self-assembled electrode wiring. In one case, the entire "T" channel void is printed and cleared (A). Once the "T" channel is cleared, a conductive fluid could be introduced to fill the vertical stem, as portrayed by the yellow portion in (D) and create an electrode channel. Next, the bacterial slurry is introduced to fill the horizontal cavity, illustrated by the blue portion in (C), to create a bacterial slurry channel.

This method leverages surface tension to achieve the separation of the fluids. A hydrophobic, conductive fluid introduced first will wet the hydrophobic vertical channel easier than an aqueous fluid such as the bacterial slurry. The bacterial slurry, introduced second in a manner such that the flow remains laminar, will have difficultly displacing the conductive fluid and will instead prefer to fill the remaining void and flow through the device. In the second case, hybrid 3-D printing would be leveraged to directly print the electrode wiring geometry using 3-D printable resin infused with conductive particles. Directly printing the wiring would simplify post processing as it would leave only the horizontal section of the "T" shaped channel, a rectangular cross-section, to be cleared of sacrificial material and then filled with the bacterial slurry.

Expanding the "T" channel concept gave way to more configuration possibilities shown in Figure 6, that pose improved efficiency and ease of fabrication.

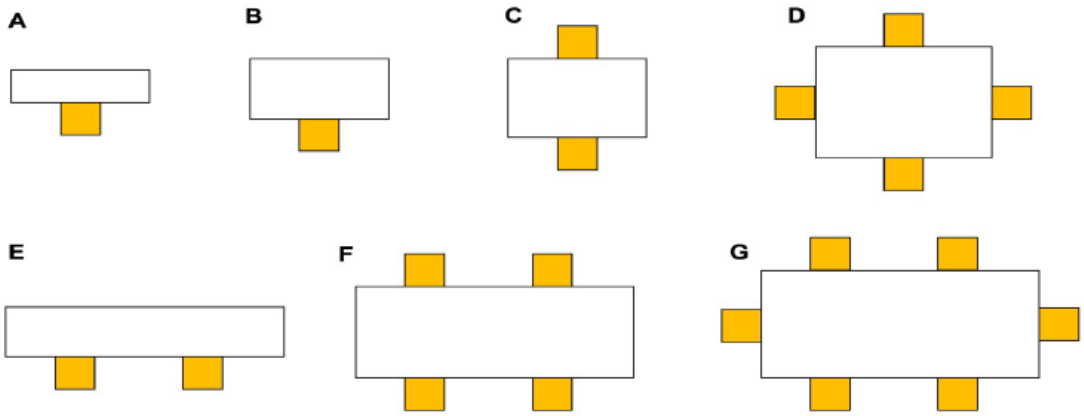

Figure 6. Expanded "T" Channel Configurations

Configurations (A-G) illustrate cross-sectional views where the white portions represent the cross-section of the bacterial slurry channels, and the yellow portions represent the cross-sections of the electrode channels. The standard "T" architecture (A) features horizontal and vertical channels of similar height. A larger horizontal channel (B) can accommodate a greater volume of bacterial slurry. Increased volume of bacterial slurry would yield increased electron generation and may also lead to a longer operational time of the device before refueling. Configurations (C) and (D) seek to optimize available volume for bacterial slurry while retaining proximity to the nearest electrode from anywhere in the volume. Configuration (E) may be appropriate for applications requiring a wide horizontal dimension with comparatively short vertical dimension. In this case, two electrodes on the same side are necessary to improve capture efficiency by retaining proximity to an electrode from anywhere in the volume. Configuration (F) is a repetition of the pattern in (C) that could be used in a larger device or as a scaling element. Configuration (G) depicts a configuration with a large bacterial slurry channel surrounded by electrode channels to support increased capture efficiency and various connectivity options as well as increased volume of bacterial slurry to improve power output.

B. MODELING AND FABRICATION

To transition the conceptualized models into a format that could be 3-D printed, Solidworks, a Computer-Aided Design (CAD) software, was utilized to render detailed

digital models that could be saved into a file format compatible with the 3-D printer. To maximize scalability, it was necessary to investigate the minimum cross-sectional dimensions of internal voids achievable by the 3-D printer used in this research.

Two designs were developed and printed for this research. The first chip design features embedded channels featuring simplified square cross-sectional geometries. These channels were used in developing and testing clearing procedures for removing sacrificial material from the embedded channels. The second chip design features embedded channels with "T" shaped cross-sectional geometries similar to Figure 6 (C), but with the electrode channels horizontally flanking the central, bacterial slurry channel. Test samples of both designs were printed with multiple, independent channels of varied cross-sectional dimensions. In all cases, the length of the channels was significantly larger than the cross-sectional dimensions. A benefit to smaller geometry between the bacterial slurry and the electrodes is a linearly scaled reduction in voltage losses due to ohmic resistance [3]. The voltage loss due to ohmic resistance has been calculated using

$$\Delta V = \frac{\delta_w I}{\sigma} \tag{2.2}$$

where δ_w, represents the distance between a reference electrode and a bipolar membrane, I represents the current density, and σ represents the conductivity of the bacterial slurry solution [3]. The size of spherical bacterial cells are generally less than 2 microns in diameter and cylindrical bacterial cells are ~ 1 micron in diameter and up to 10 microns in length [9]. The concentration of bacteria within the MFC, along with available food source, impact how much energy can be generated by the bacteria and thus harnessed by the MFC. This leads to an inverse relationship between the available volume for the bacterial slurry and the distance between the furthest points in the volume and the nearest electrode. Testing for the minimum achievable internal cross-section will determine the lower limit for work in optimization of the geometry.

The dimensions planned for and investigated for the square cross-section channels were as follows: 64, 96, 192, 288, 384, 512, 608, 704, 800, 896, and 992-microns square; the octal variation was chosen to complement the minimum pixel-size capability of the

printer and thereby reduce uncertainty in printing fractional pixel-sizes. This range was expected to determine the minimum dimensions achievable by the printer while sweeping through a relevant range of dimensions for MFC architectures to include dimensions comparable to the ~100-micron dimension used in the 2019 NPS research.

The dimensions investigated for the "T" based architecture include two bacterial slurry channel dimensions and five flange dimensions. The two bacterial slurry channel cross-section dimensions investigated were 192-microns square and 288-microns square. The five cross-section dimensions investigated for the flanges are 32, 64, 96, 128, and 160-microns square. The 32-micron square flange dimension was expected to be too small to be created successfully on its own but may be possible when paired with the larger bacterial slurry channel. The bacterial slurry channel dimensions chosen for the "T" based architecture are comparable to the ~100-micron dimension used in the 2019 NPS research when considering the distance from any point within the bacterial slurry channel to the nearest flange. The overall chip dimensions were 9cm long, 7cm wide, and 2.2mm tall with a 3.1mm tall rim. The sample chips feature 650-micron diameter ports for accessing the channels. These ports were designed to accommodate a 1cc, luer tipped syringe.

The printer utilized was the Stratasys Objet500 Connex which has a print volume of approximately 0.03822 cubic meters and is capable of printing multiple materials in a single print run. The Objet500 Connex printer works by the concept of PolyJet 3-D printing, whereby layers of ultraviolet (UV) light sensitive resins are deposited in layers which are cured by exposure to UV lamps collocated on the print head. The primary structural material used for this research was VeroClear-RGD810. The sacrificial material used was SUP706. The dark material used in the dark reference channels was Agilus30 Black FLX985. The VeroClear material is rigid after printing and nearly transparent, ideal for verification of structural formation and function during testing. The sacrificial material is translucent and is soluble in sodium hydroxide (lye).

For the printer used in this research, an existing conductive resin was not commercially available. Custom-made conductive resins used in PolyJet printing have conductive micro-spheres, nanoparticles, or other small scale conductive media diffused throughout a light-sensitive resin. Such materials are printable but not in a hybrid mode;

they must be custom printed one at a time, at low resolution. As a result, the available geometries are extremely limited, typically only featuring simple, single level 2D devices.

Once printing was complete, the sacrificial material needed to be removed from the channels to prepare the chips for testing and verification. The sacrificial material, SUP706, is recommended by the printer manufacturer, to be removed by a combination of manual handling, water-jetting, and exposure to sodium hydroxide (lye). Water-jetting was determined to be inappropriate for this research due to the small geometries. Manual removal by hand, exposure to lye, and gravity draining supported with heating were tested in this research and used to develop a procedure for repeatable clearing of the channels. The procedure developed over the course of this research and used for clearing the channels is presented in Table 1.

Table 1. 3-D Printed Miro-Channel Clearing Procedures

3-D Printed Micro-Channel Clearing Procedures	
1	Hand clean to remove exterior sacrificial material. No chemicals.
2	Place chip in 10% NaOH solution and sonicate for 1 hour.
3	Remove chip from sonication bath and 10% NaOH solution.
4	Rinse chip with fresh water.
5	Orient chip to promote gravity drainage and bake at 80 °C for 4 hours.
6	Remove chip from heat and allow to cool to room temperature.
7	Flush each channel with 10% NaOH solution using syringe with luer tip.
8	Rinse chip with fresh water.
9	Flush each channel with fresh water.

C. DESIGN TESTING

To determine the degree of success for creation of the interior channels for both the square and “T” shaped channel configurations after printing and post-processing, a relativistic analysis was conducted. For this analysis, images of each respective channel were taken under a microscope and compared to a reference channel of the same characteristics from a purpose printed reference chip. For each channel geometry and dimension tested per sample chip, four images were taken and analyzed and the averages

of those four images were compared. Standard deviation data for each data series was obtained for determinations of consistency and use in follow on analyses. This approach helps to mitigate the impact of outliers in the sampling to obtain general results that could indicate measures of repeatable future results. In total, 12 sample images per dimension were analyzed and compared to their respective reference average to determine the relative clearance of each channel.

The images were taken using an AmScope microscope and ISCapture software. The images of the channels used in the relative clearance analysis were taken as viewed from above with a total optical magnification factor of 3.15. The software added additional digital magnification with some loss of resolution. The combined magnifications led to a 64-micron wide channel appearing to be approximately 20.016mm across when viewed on the computer monitor.

The reference samples featured the same respective channel characteristics but utilized a dark colored resin for printing the internal features. The reference samples did not feature access ports to ensure the channels remained filled over time and through handling. The images were uploaded into AutoCAD where the regions of interest could be digitally traced, and a numerical quantity of the traced area could be obtained. For the reference channels, the traced area was the dark colored sections and for the test samples, the traced area was the sections perceived to be cleared. The numerical quantities for the respective areas were then compared to determine the level of success for the creation of the desired internal structures. This analysis provides results of success relative to the respective references. Channel width measurements were taken to determine what actual widths of the completed channels to obtain information about how well the desired dimensions corresponded with actual created structures.

For the square cross-section samples, additional analyses were conducted to better identify trends in fidelity and repeatability for the creation of the desired channels and their respective dimensions. For these analyses, measurements were obtained by use of the ISCapture software's measurement tool. The software's measurement tool was calibrated using an image of a stage micrometer posing 10-micron graduations taken under the same conditions as the width measurements. Following calibration, five width measurements

were taken for each of the three sample chips channels' including cleared channels and their respective, on chip, wax references. Five width measurements were also taken of each dark resin reference channel and their respective, on chip, wax references for the purpose printed reference chip. From these measurements, relationships between desired dimensionality and measured dimensionality were obtained along with respective averages and standard deviations. These metrics were used to support determinations of dimensional fidelity and repeatability for this manufacturing process. Additionally, the results from the relative clearance analysis were combined with results of this analysis to obtain quantifiable data for the true clearance percentages of the square channels. This analysis also included the propagated uncertainty data for the clearance percentages.

To determine if the "T" shaped cross-sectional channels were successful at achieving the self-assembled wiring effect, a color dyed, oil-based substance was injected to fill the entire cavity, electrode channels and bacterial slurry channel, and then fresh water was introduced to flush the dyed substance from the central, bacterial slurry channel. The surface tension within the channels and hydrophobic nature of the dyed substance is expected to enable the substance to remain within the electrode channels while the water replaces the dyed substance within the bacterial slurry channel section. Observations of color intensity variation, as viewed from above through the microscope, were then noted, with success being indicated by darker outer edges and lighter or clear central channels. The magnification factor was adjusted during these analyses to obtain the best view and a stage micrometer was used to obtain width measurements for respective images.

III. RESULTS

This chapter presents the results obtained for the fabrication and testing of the square and "T" shaped channel architectures. Section A of this chapter presents the results for the square cross-section channels. Sections B and C present the results for the "T" shaped cross-section channel experiments. Elements addressed in this chapter include the degrees of success for 3-D printing and clearing of the envisioned internal architectures and self-assembled wiring in the case of the "T" based architectures.

For both the square and "T" based cross-section designs, three test samples were created and compared to their respective references. In total, eight chips were analyzed, four for the square cross-section configuration and four for the "T" based cross-section configuration. This chapter is organized to first present the square geometry results. Next, the "T" shaped channel results for the planned 192-micron square bacterial slurry channel with "T" flange geometry are presented and followed by the planned 288-micron square bacterial slurry channel with "T" flange geometry results. Finally, the self-assembled wiring experiment results utilizing the "T" based architecture channels are shown.

A. SQUARE CROSS-SECTION FABRICATION AND CLEARING

For the square cross-section samples, the cross-section dimensions were varied to determine the minimum dimension achievable by the printer and post-print processes used in this research. The upper limit, 992-microns square, was chosen to allow for sufficient variation within the envisioned employment scales. The planned dimensions evaluated in the square cross-section samples were height and width values as follows: 64, 96, 192, 288, 384, 512, 608, 704, 800, 896, and 992-microns. Figure 7 depicts the completed SolidWorks rendering and a 3-D printed and processed sample chip featuring the square cross-section channels. In these images, the completed channels are beneath the access ports and a sealed reference channel, filled with sacrificial material, is to the right of each respective channel for immediate visual comparison. The channel dimensions being tested are increasing from left to right on each chip.

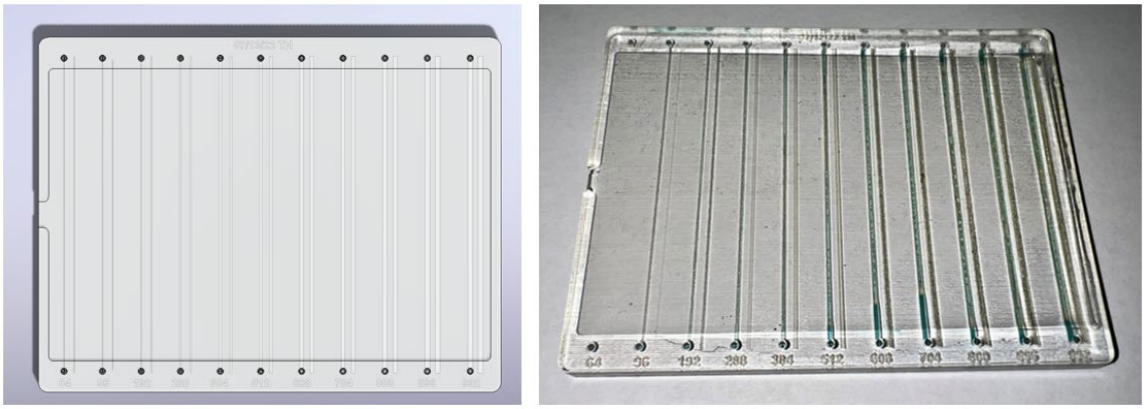

Figure 7. Square Cross-Section Chip: SolidWorks Rendering (Left), 3-D Printed and Processed (Right)

Figure 8 displays the square channel reference chip along with a printed and post-print processed sample chip. The reference channels are the dark colored channels printed to the right of a corresponding channel filled with sacrificial material. The sample chip channels that were cleared and compared to their respective references are the channels directly below the ports on the sample chip. This chip also poses sealed reference channels to the right of each test channel. These reference channels were created with the sacrificial material and not the dark colored resin used for the references which were used in the data collection and processing.

The sample dimensions are increasing from left to right on these chips beginning with the planned 64-micron channels on the left and ending with the planned 992-mircon channels on the right. From the images in Figure 8 it can be seen in some cases, particularly in the smaller dimension channels, the width of the cleared channels on the sample chip appears wider than the corresponding channel on the sample chip.

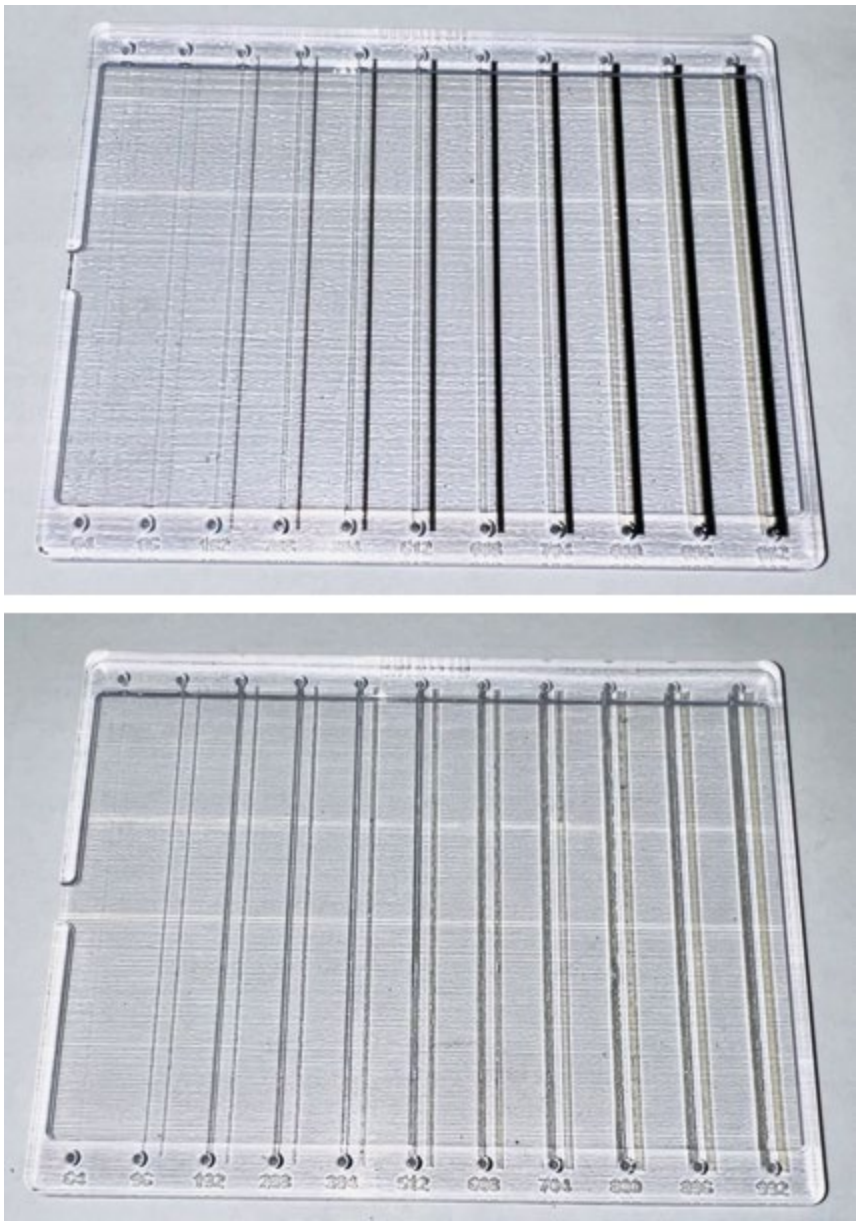

Figure 8. Square Shaped Channels Reference (Top) and Sample Chip (Bottom)

Table 2 presents the average relative clearance percentages across the three respective sample channels per cross-section dimension and their associated standard deviations. The planned 192-micron dimension had the highest average clearance percentage at 95%, with the second highest average standard deviation, 32%. The average relative clearance percentage across all of the samples, excluding the 64-micron channels

which did not succeed in any trial, is 76% with an associated average standard deviation of 24%.

Table 2. Square Cross-Section Average Relative Clearance Percentages and Standard Deviations by Cross-Section

Square Chip Totals		
Planned Cross-Section Dimensions [μm]	Average	Standard Deviation
64	0%	0%
96	26%	38%
192	95%	32%
288	82%	32%
384	70%	27%
512	84%	20%
608	74%	22%
704	83%	20%
800	82%	13%
896	89%	18%
992	76%	21%

Figure 9 presents the relative clearing percentages for each respective measurement from the square cross-section sample channels across each respective cross-sectional variation collected from the three printed samples compared against the reference sample. The relative clearance trend line is also included. Relative clearance percentages greater than 100% were observed which agrees with the visual observations of some cleared channels appearing wider than their respective references. The 64-micron channel samples did not succeed in any trial and are included in this data at a value of zero. Potential causes for this phenomenon are discussed in Chapter IV.

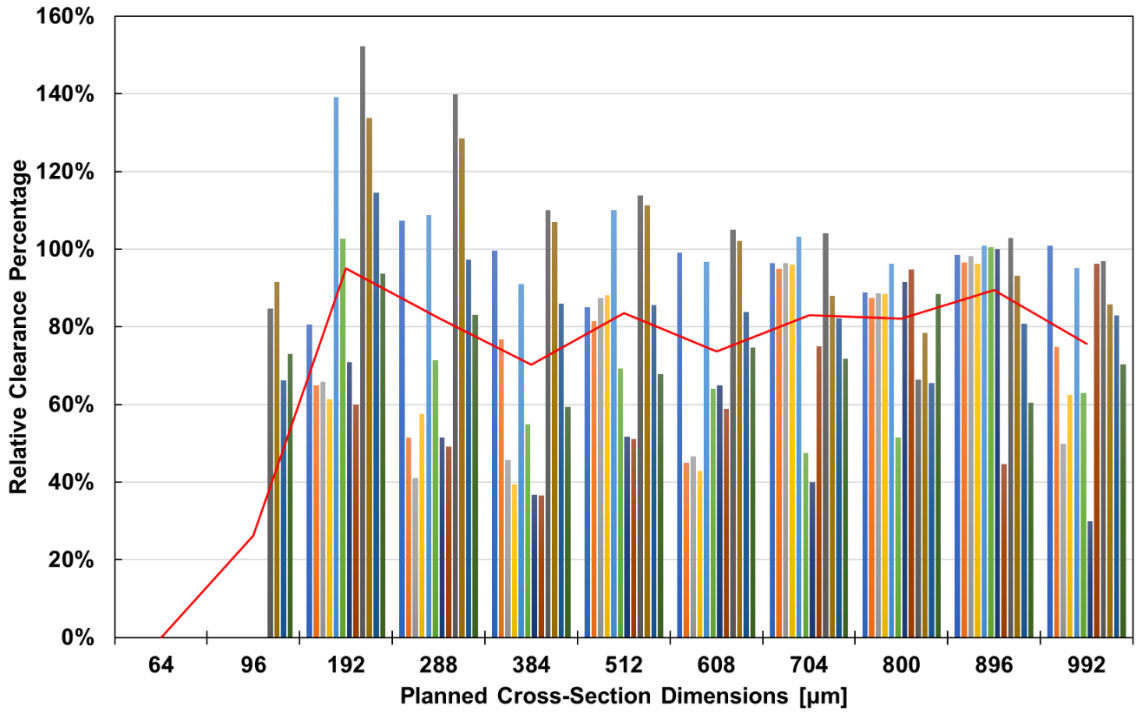

Figure 9. Square Cross-Section Relative Channel Clearance Percentages with Trendline

Figure 10 highlights the clearance percentage trendline with the standard deviation data associated with each respective cross-section dimension analyzed. The general trend appears to show that the standard deviation per cross-sectional dimension decreases as the dimensions increase. The 64-micron channel samples did not succeed in any trial and are included in this data at a value of zero.

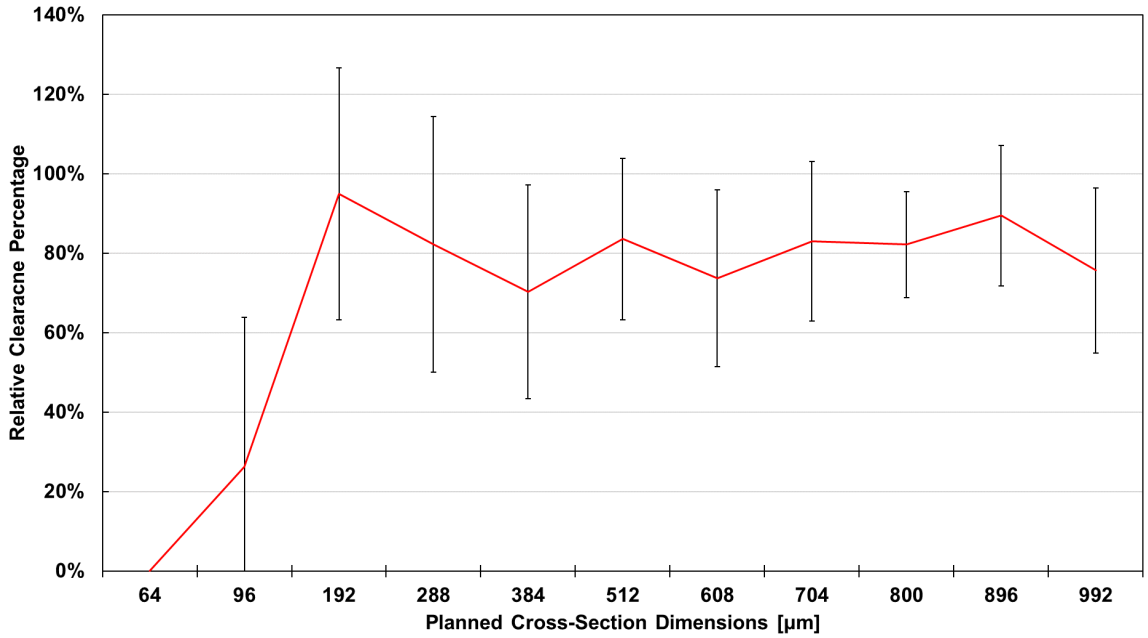

Figure 10. Square Cross-Section Relative Channel Clearance Percentages Trendline with Standard Deviations

From the data in Table 2, Figure 9, and Figure 10 it can be seen that clearance percentages greater than 100% were observed. This is because the channels printed larger than planned in many cases. To obtain true clearance metrics compared to each channel's respective actual size, width measurements were taken for each respective channel and used to normalize the data. Figure 11, 12, and 13 present the results from the width measurements and normalized clearances.

Figure 11 presents the planned channel widths versus the measured averages and respective standard deviations for each channel printed across the four chips that pose the square cross-section channel geometry. A reference line with a slope of one is included to show ideal behavior. The measured widths were larger than the planned widths for almost all cases. The smallest dimension measured to be ~ 200-microns and came from the smallest planned dimension successfully created and cleared, 96-microns. The standard deviations in this data generally decrease with increasing dimensionality.

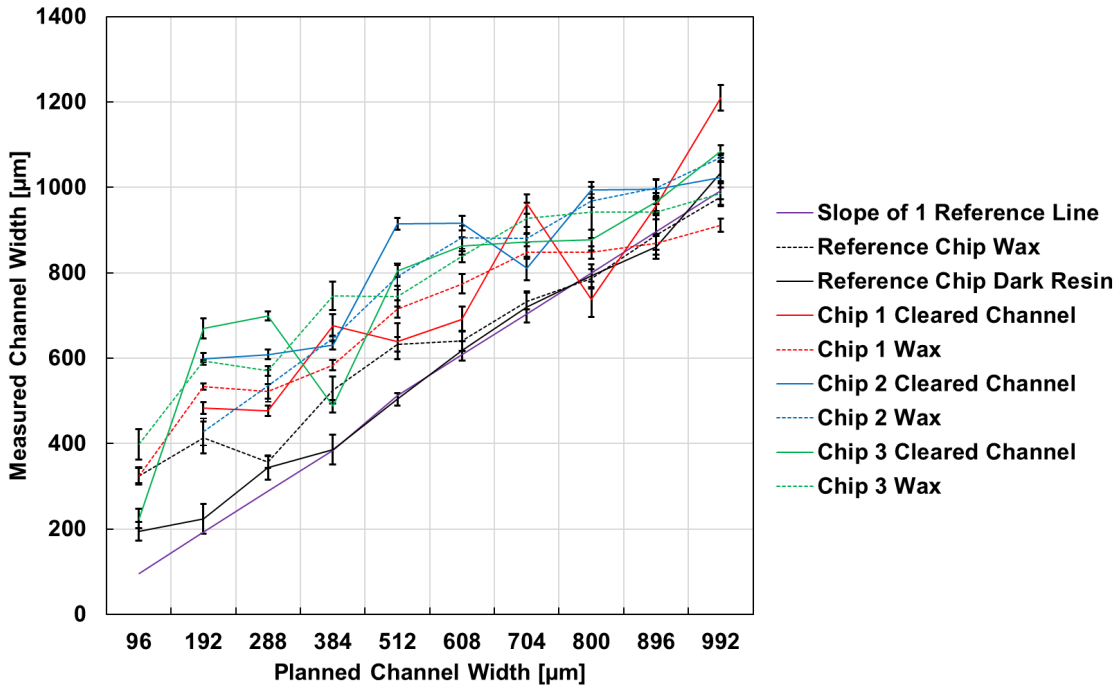

Figure 11. Planned Channel Width versus Measured Width Averages with Standard Deviations

Figure 12 presents the measured channel width for a single data point from each cleared channel for each respective chip with square cross-section channels versus their respective clearance percentage. The data points represent the average of the measurements associated with each width measurement series. The clearance percentage was obtained by multiplying the relative clearance percentages by the ratio of the dark resin channel width over the cleared channel measured width. The horizontal error bars correspond to the standard deviation of the measurements for each respective channel dimension per chip. The vertical error bars represent the percentile error obtained from calculating the propagated errors from the relative clearance analysis and the width measurement analysis. Calculated clearance percentages greater than 60 percent appear repeatable for geometries greater than 700-mircons. In smaller dimensions, some cases yielded high clearance percentages but with less consistency and predictability.

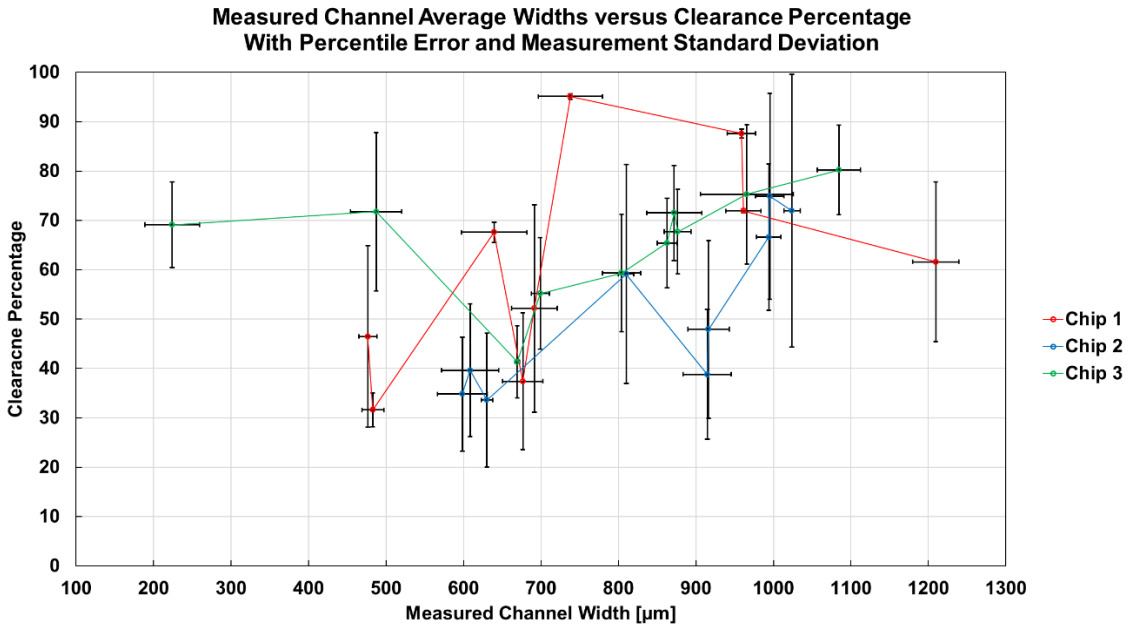

Figure 12. Average Widths of Measured Channels versus Clearance Percentage with Percentile Error and Measurement Standard Deviation

Figure 13 presents the measured channel width versus clearance percentage for a single data point for each channel printed and cleared. The data points represent the average for each respective set of channel measurements. The horizontal error bars correspond to the standard deviation of the width measurements for the respective measurement series. The vertical error bars represent the percentile error obtained from calculating the propagated errors from the relative clearance percentage analysis and the width measurement analysis.

This presentation is independent of any single chip and is intended to show general trends for measured width dimension versus clearance percentage with the respective error bars being indicative of expected repeatability. The measured dimensions greater than 700-microns demonstrate reasonable repeatability in achieving clearance percentages of at least 60%. The smaller measured dimensions demonstrated instances of high clearance percentages but with less consistency and predictability. It was not clear as to what type of dependence relationship between channel clearance percentage and channel width could be expected and so an accurate fitting curve was not incorporated into this data set.

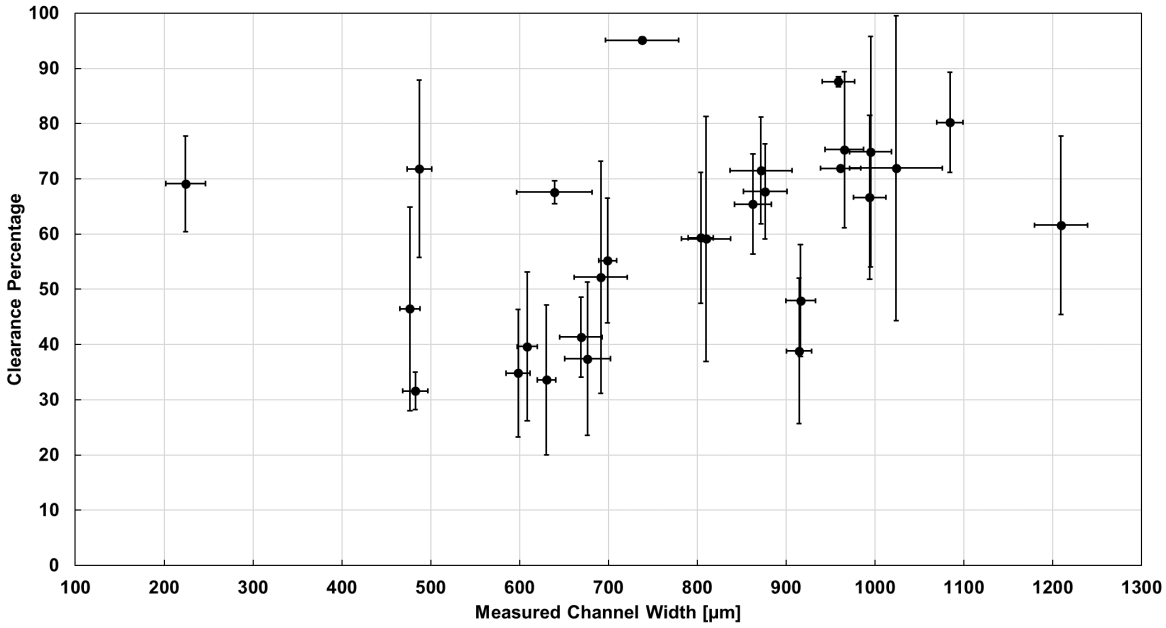

Figure 13. Average Widths of Measured Channels versus Clearance Percentage with Measured Width Standard Deviation and Clearance Percentage Percentile Error

Figure 14 presents a collage of images to illustrate some of the variations seen and methods used in this research. The images for the planned 192-micron and 992-micron channels were specifically chosen for this collage as they best highlight the observed trend of higher uncertainty and lower fidelity in the creation of the smaller dimensions compared to the larger dimensions tested. In the planned 192-micron samples shown, it is clear that the actual measured dimension of the channel's width is much greater than intended. This disparity is less prevalent in the planned 992-micron channels. Images E and F also illustrate the uncertainty in tracing the true edges of the channels which incorporated uncertainty in the relative clearance percentage analyses.

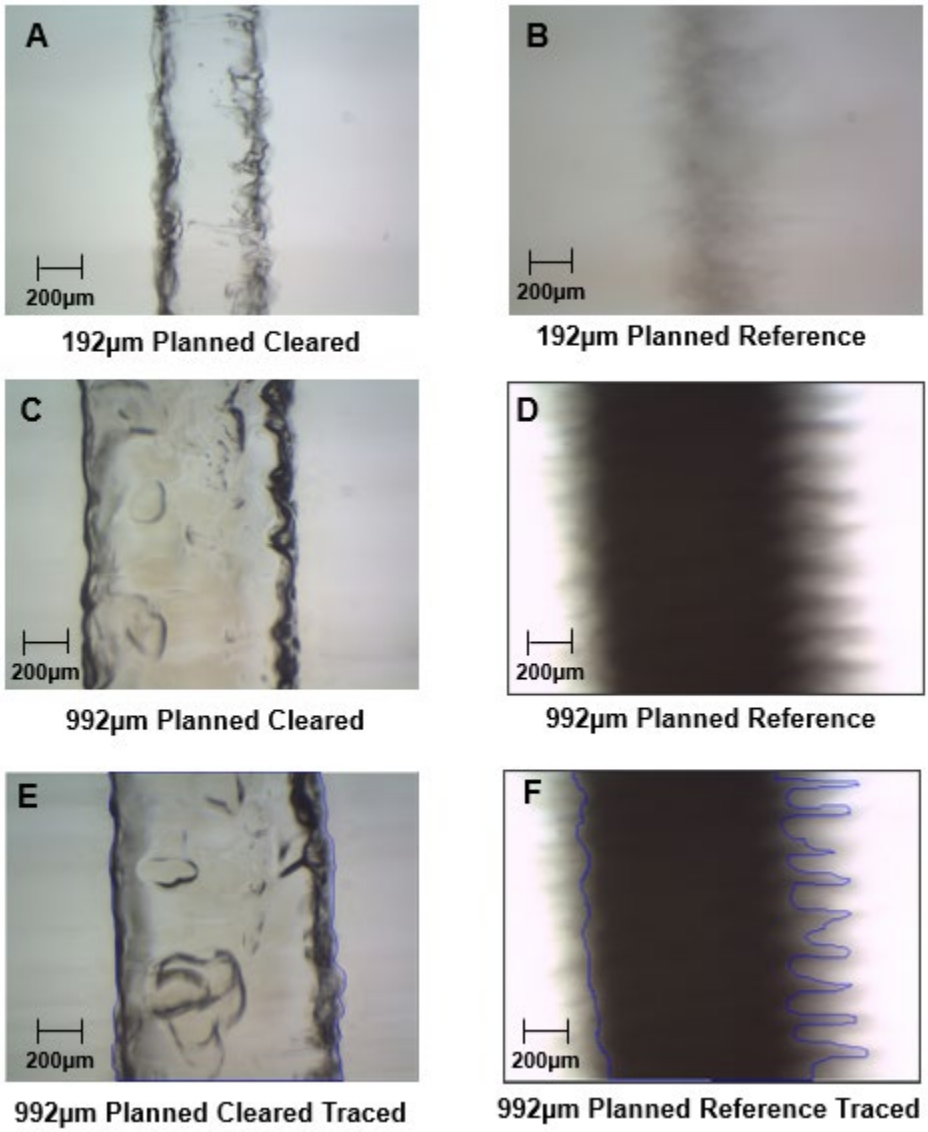

Image A is a planned 192-micron channel after being cleared. Image B is a planned 192-micron reference channel printed in dark resin. Image C is a planned 992-micron channel after being cleared. Image D is a planned 992-micron reference channel printed in dark resin. Images E and F display planned 992- micron examples of a cleared channel (E) and a dark resin reference (F) with the trace lines used in the clearance analyses.

Figure 14. Collage of Cleared Channels (Left) and Corresponding Dark Resin Reference Channels (Right)

B. "T" SHAPE BASED CROSS-SECTIONAL ARCHITECTURE

For the "T" shape-based cross-section samples both the dimensionality of the larger central channel, called the bacterial slurry channel, and the smaller channels meant to support the wiring, called the electrode channels or flanges were varied. Two planned bacterial slurry channel cross-section dimensionalities were tested, 192-microns and 288-microns square. The planned electrode channel cross-section dimensionalities tested were as follows: 32, 64, 96, 128, and 160-microns.

Figure 15 shows the "T" shaped channel reference chip and a printed and cleared "T" shaped channel sample chip. The reference channels are easily visible due to the high color contrast between the dark resin used to print the channels. The five channels on the left half of the chips pose the planned 192-micron bacterial slurry channel dimension with secondary dimensionalities increasing from left to right. The five channels on the right half of the chips pose the planned 288-micron bacterial slurry channel dimension with secondary dimensionalities increasing from left to right. It is again observed that some of the cleared channels appear visually wider than their respective references.

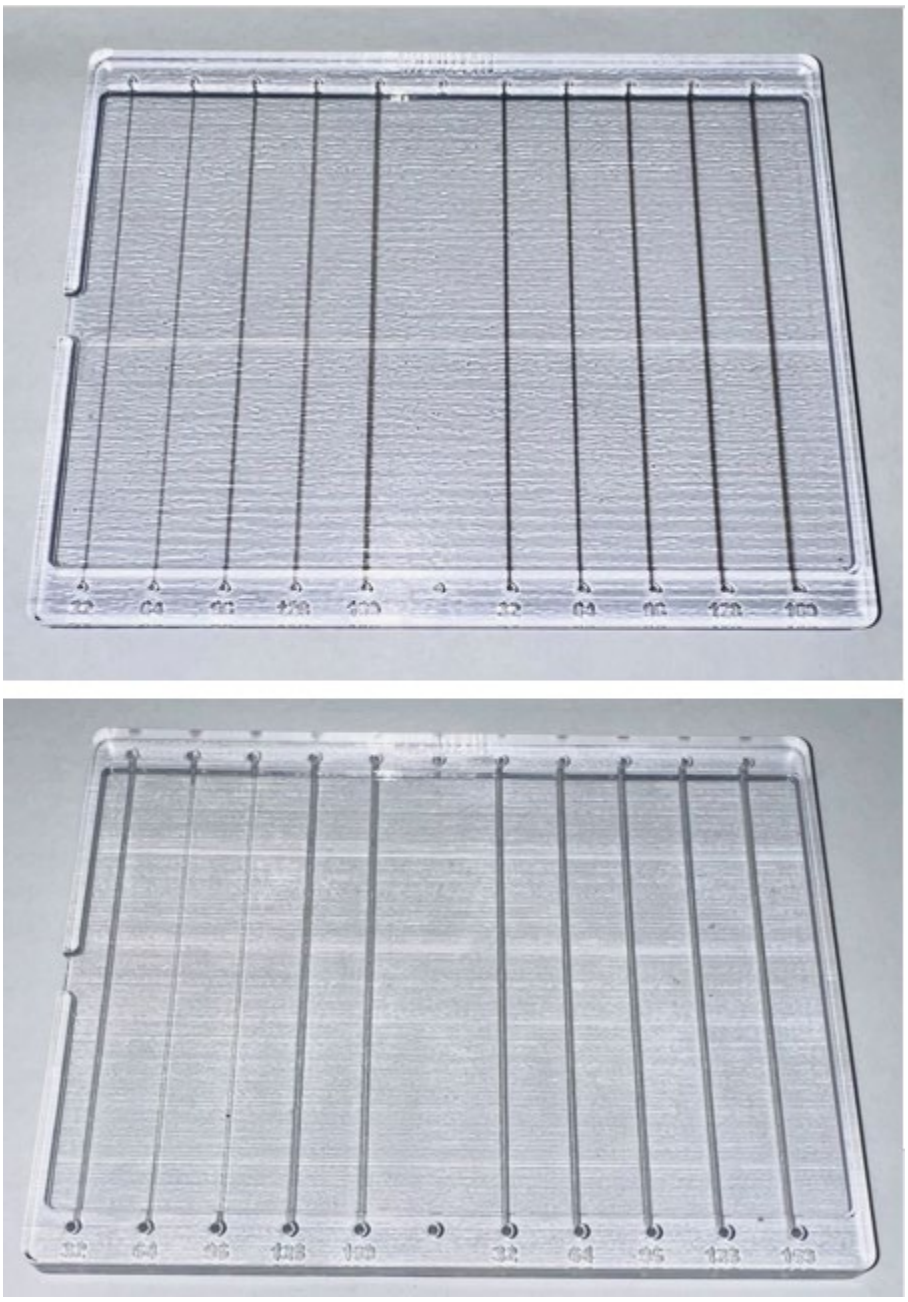

Figure 15. “T” Shaped Channels Reference (Top) and Sample Chip (Bottom)

Figure 16 exhibits conceptualizations of the embedded “T” shaped channels. (A) shows the entire printed channel empty. (B) shows the entire channel filled with the medium to become wiring. (C) shows the channel after flushing with water and emphasizing the flanges remain filled with the conductive medium to create self-assembled wiring within the channel.

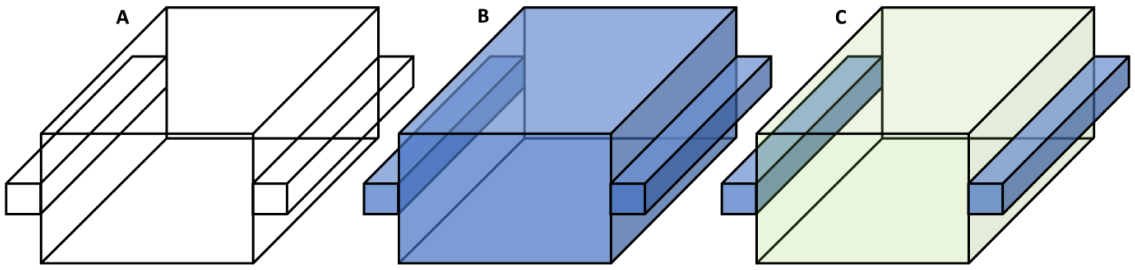

(A) is the "T" shaped channel empty. (B) shows the "T" shaped channel filled with the medium to make up the self-assembled wiring. (C) shows the channel after flushing and highlights that the flange channels remain filled with the conductive medium creating self-assembled wiring.

Figure 16. Embedded "T" Shaped Channel Architecture

Table 3 presents the average relative clearance percentages across the three respective sample channels per cross-section dimension and their associated standard deviations. The relative clearance percentage values greater than 100% agree with the observation that the some of the cleared channels appear wider than their corresponding references.

The total average relative clearance for the planned 192-micron primary dimension series is 100% with a standard deviation of 25%. The planned 64-micron flange dimension had the highest relative clearance percentage average at 130%, with the highest average standard deviation at 41% for the planned 192-micron bacterial slurry channel samples.

The planned 288-micron primary dimension series has a total average relative clearance of 114% with an average standard deviation of 17%. The planned 128-micron flange dimension had the highest relative clearance percentage average at 120%, with an average standard deviation of 15% for the planned 288-micron bacterial slurry channel samples.

Table 3. "T" Shaped Cross-Section Average Relative Clearance Percentages and Standard Deviations by Cross-Section

"T" Chip Totals		
Planned Cross-Section Dimensions [μm] Primary_Flange	Average	Standard Deviation
192_32	92%	20%
192_64	130%	41%
192_96	96%	25%
192_128	102%	20%
192_160	80%	21%
--------	--------	--------
288_32	109%	21%
288_64	116%	14%
288_96	107%	19%
288_128	120%	15%
288_160	115%	16%

Figure 17 displays the relative channel clearance percentage data and trendline for the "T" shaped cross-section architecture samples featuring the planned 192-micron bacterial slurry channel dimension.

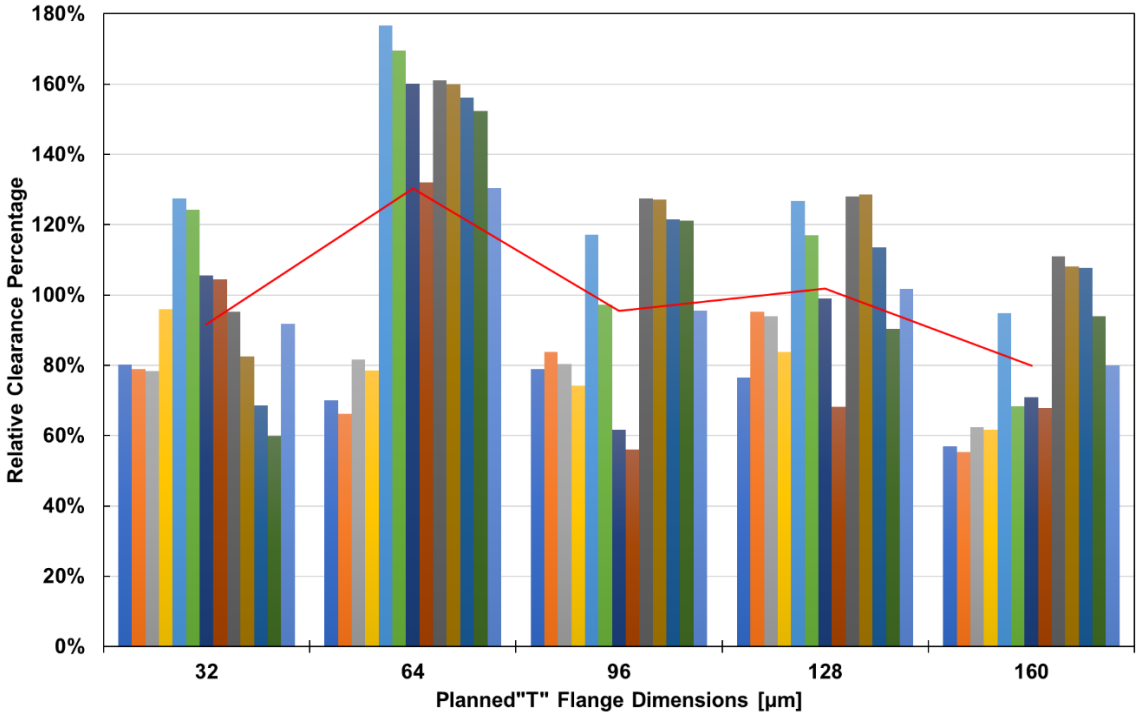

Figure 17. "T" Shaped Cross-Section Channel Dimensions versus Relative Clearance Percentages with Trendline for Planned 192-Micron Bacterial Slurry Channel Dimension

Figure 18 highlights the planned dimension versus relative clearance percentage trendline with associated standard deviations from the "T" shaped samples featuring the planned 192-micron bacterial slurry channel dimensions. From these results a high degree of repeatability can be expected from the fabrication processes utilized in this research in creating these channels. Further analyses and experimentation will need to be conducted to improve the dimensional fidelity of these channels and features.

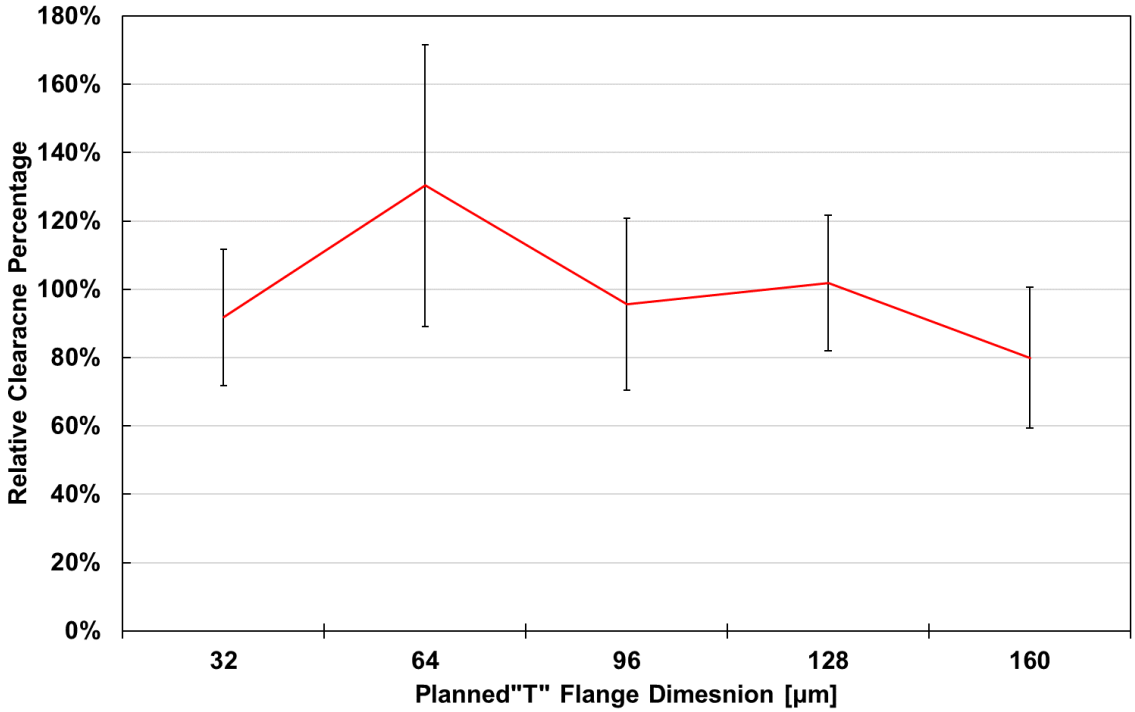

Figure 18. Trendline for "T" Shaped Cross-Section Channel Dimensions versus Relative Clearance for Planned 192-Micron Bacterial Slurry Channel Dimension

Figure 19 displays the channel relative clearance percentage data and trendline for the "T" shaped cross-section architecture samples featuring the planned 288-micron bacterial slurry channel dimension.

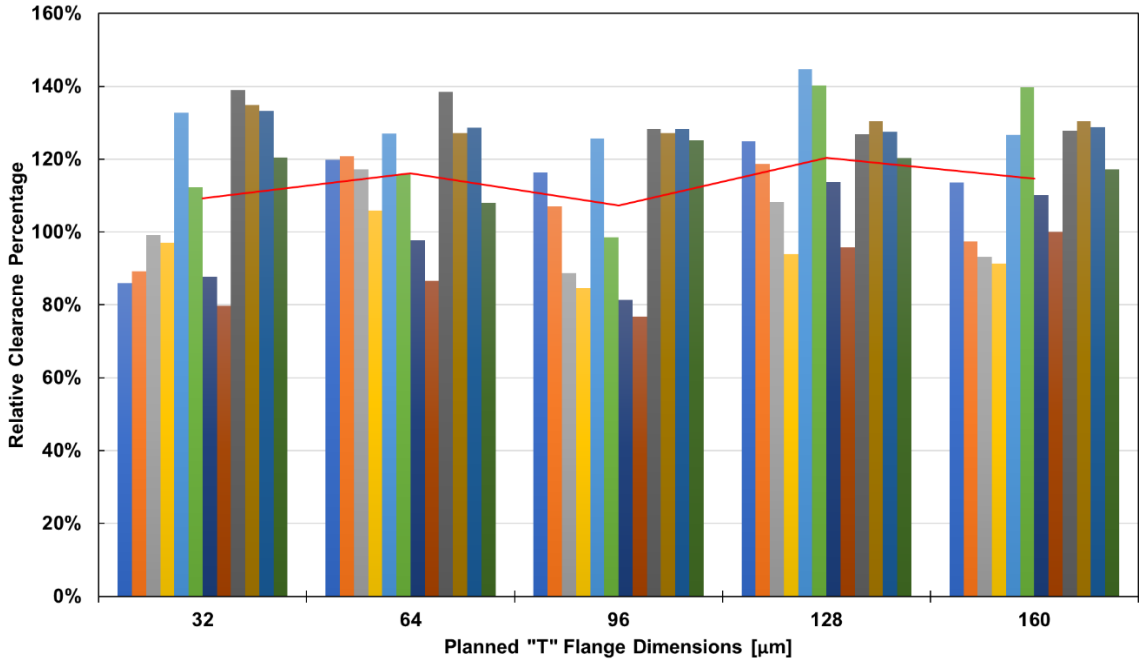

Figure 19. "T" Shaped Cross-Section Channel Dimensions versus Relative Clearance Percentages with Trendline for Planned 288-Micron Bacterial Slurry Channel Dimension

Figure 20 highlights the trendline and associated standard deviations from the "T" shaped samples featuring the planned 288-micron bacterial slurry channel dimensions. From these results it is concluded that a high degree of repeatability can be expected from the fabrication processes used in this research. Additional experimentation and analyses are required to improve the dimensional fidelity of the channels and features.

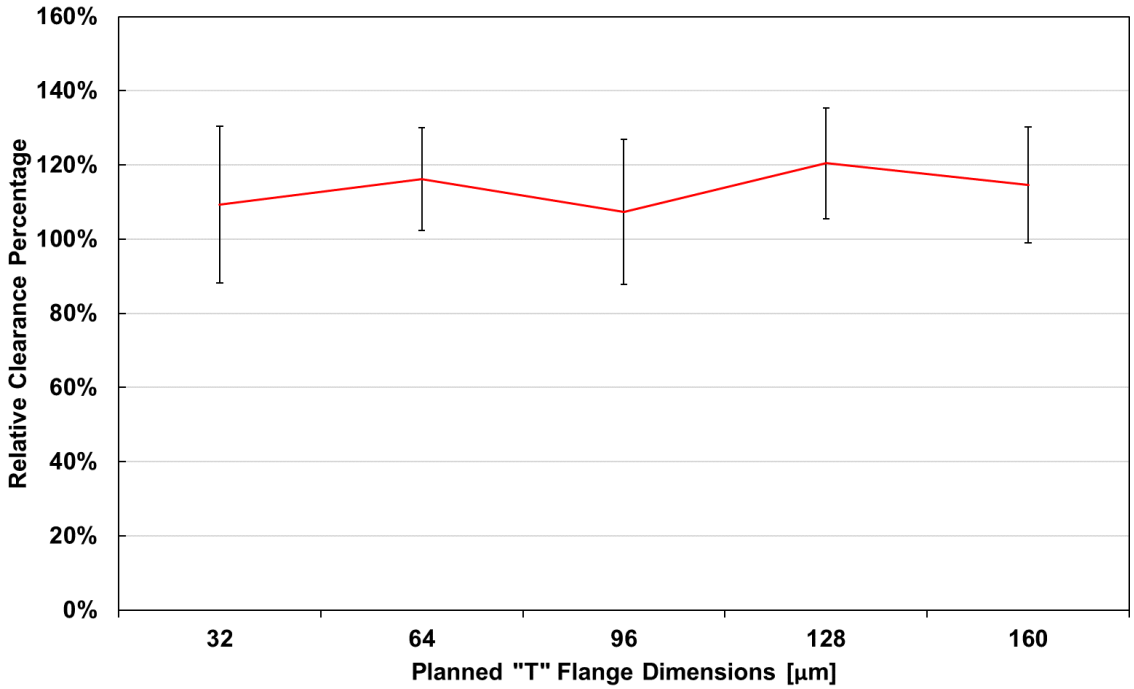

Figure 20. Trendline for "T" Shaped Cross-Section Channel Dimensions versus Relative Clearance for Planned 288-Micron Bacterial Slurry Channel Dimension

C. SELF-ASSEMBLED WIRING

Self-assembled wiring for this application is created by the entrapment of a hydrophobic material in the "T" flange cavities. The fluidic surface tension will hold the material in place while the bacterial slurry channel is flushed with water. The hydrophobic nature of the material used to represent the wiring ensures the material will not mix with the water in the bacterial slurry channel.

To determine if the "T" shaped channel geometries are capable of supporting self-assembled wiring, an oil-based dyed substance was introduced into the channels and then fresh water was introduced to flush the channel. Success of self-assembled wiring concept to be indicated by blue colored channel edges with a lighter blue or clear central channel. The dyed substance used was vegetable oil mixed with Winsor and Newton, Winton Oil Colour, Prussian Blue paint at an approximate ratio of 5.42:1 determined by weight. Across

the 10 “T” based geometry variations tested during this research, 6 variations yielded the desired effect.

Consistent with the previous analyses, three chips were analyzed. The planned 192-micron bacterial slurry channels featuring planned 32, 64, 96, and 128-micron flanges clearly portrayed the desired fluid separation effect in at least one of the samples tested. The planned 288-micron bacterial slurry channels featuring planned 32-micron and 64-micron flanges clearly portrayed the desired fluid separation effect in at least one of the samples tested.

Figure 21 displays the planned 192-micron bacterial slurry channel dimension samples that demonstrated successful fluid separation within the respective channels. The measured widths of these channels were greater than the planned dimensions similar to the results obtained in the square channel analyses. There are a variety of factors that can impact the self-assembled wiring effect demonstrated here. Some of these factors are discusses in Chapter IV. Further experimentation and analyses are required to improve the dimensional fidelity in the fabrication process.

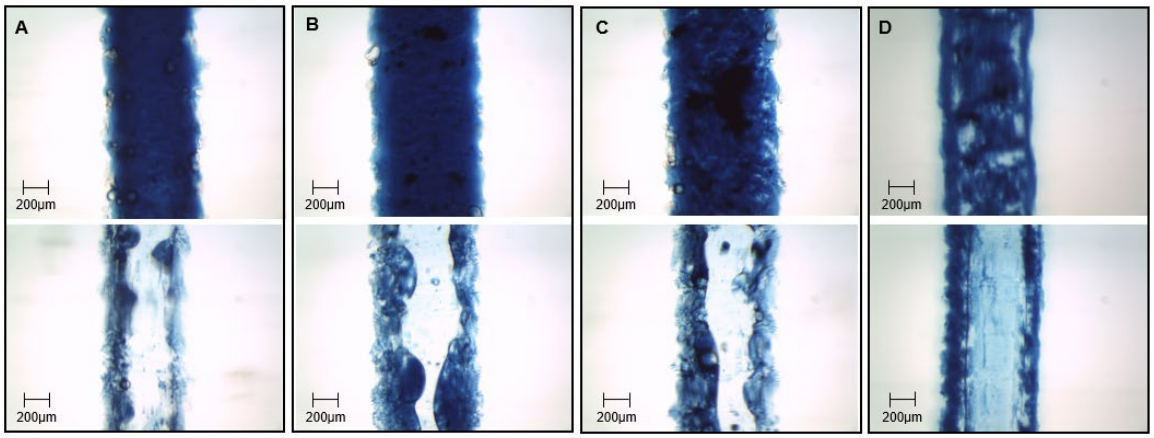

Successful sample channels for the planned 192-micron bacterial slurry channel dimensions with “T” flange dimensions of 32, 64, 96, and 128-microns, corresponding to groupings A, B, C and D respectively. The top image for each grouping shows the respective channel filled with the dyed oil and the bottom image shows the respective channel after being flushed with fresh water.

Figure 21. Self-Assembled Wiring Concept Proof for Planned 192-Micron Bacterial Slurry Channel Dimension

Figure 22 displays the planned 288-micron bacterial slurry channel dimension samples that demonstrated successful fluid separation within the respective channels.

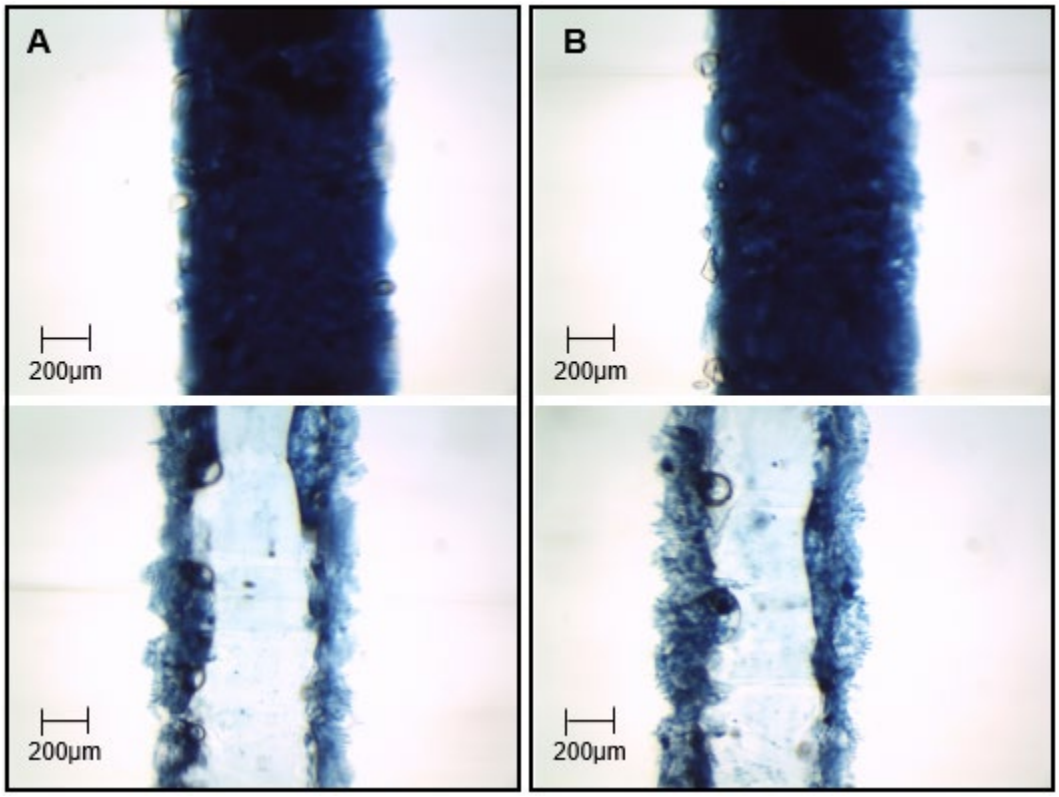

Successful sample channels for the planned 288-micron bacterial slurry channel dimensions with "T" flange dimensions of 32-microns (A) and 64-microns (B). The top image for each grouping shows the respective channel filled with the dyed oil and the bottom image shows the respective channel after being flushed with fresh water.

Figure 22. Self-Assembled Wiring Concept Proof for Planned 288-Micron Bacterial Slurry Channel Dimension

Figure 23 depicts images from the cases that were determined to be unsuccessful in achieving the fluid separation effect necessary to support self-assembled wiring.

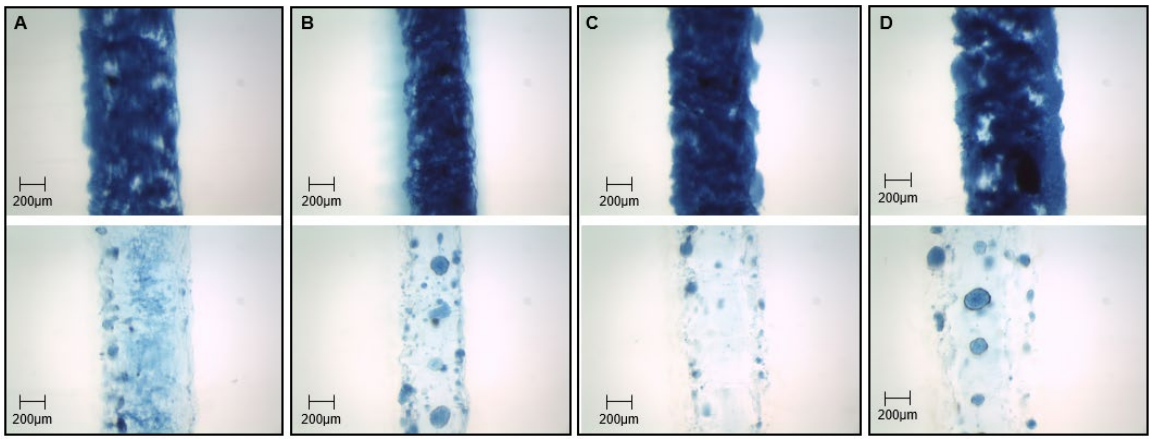

Unsuccessful sample channels for the planned 192-micron bacterial slurry channel dimension with planned 160-micron flanges (A), planned 288-micron bacterial slurry channel dimension with planned 96-micron flanges (B), planned 288-micron bacterial slurry channel dimension with planned 128-micron flanges (C) and planned 288-micron bacterial slurry channel dimension with planned 160-micron flanges (D). The top image of each grouping shows the respective channel filled with the dyed oil and the bottom image shows the respective channel after being flushed with fresh water.

Figure 23. Unsuccessful Cases for Self-Assembled Wiring Concept

D. "Y" MERGER FOR UPSCALING THE "T" SHAPED CHANNEL ARCHITECTURE

The results presented in the previous sections are encouraging but to increase the scale of power harnessed from MFCs, multiple channels must be arrayed to create a scaled up BMFC. Successful arraying of these channels requires that there be no discontinuities of the electrodes from the contributing channels. Figure 24 and Figure 25 illustrate unsuccessful and successful conceptualizations of architectures for multiple channel arraying respectively.

Figure 24, illustrates a discontinuity in the electrodes (yellow) from two horizontally configured bacterial slurry channels (blue). The discontinuity would inhibit electricity flow from the electrodes at the channel to other portions of the device and ultimately to an electric load.

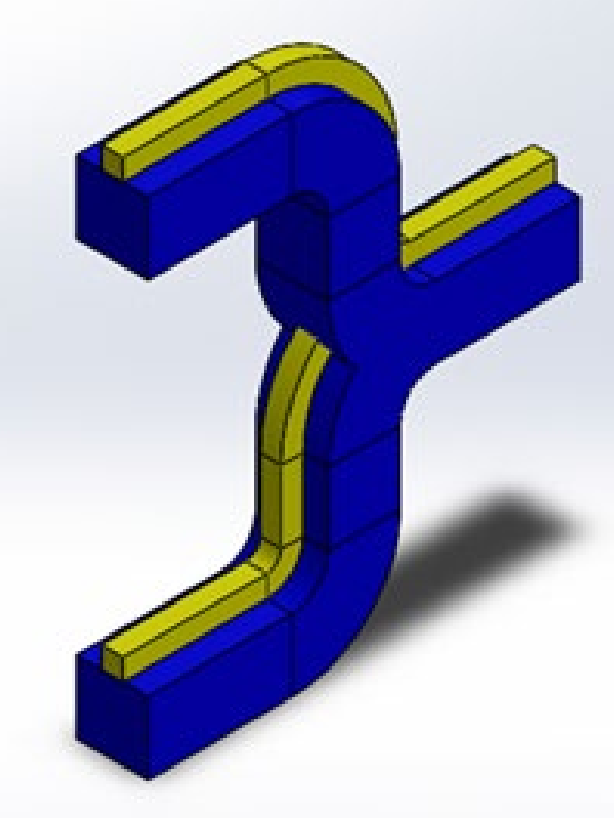

Figure 24. Electrode Discontinuity in Multidimensional Channel Array.

One method to avert discontinuities and achieve a successful multidimensional array of channels is illustrated by Figure 25 where the electrode channels (yellow) supporting electron harnessing from two separate bacterial slurry channels (blue) can be merged using a 3-D "Y" or yoke-like configuration. This would allow uninterrupted electron flow throughout the device enabling scalable power generation.

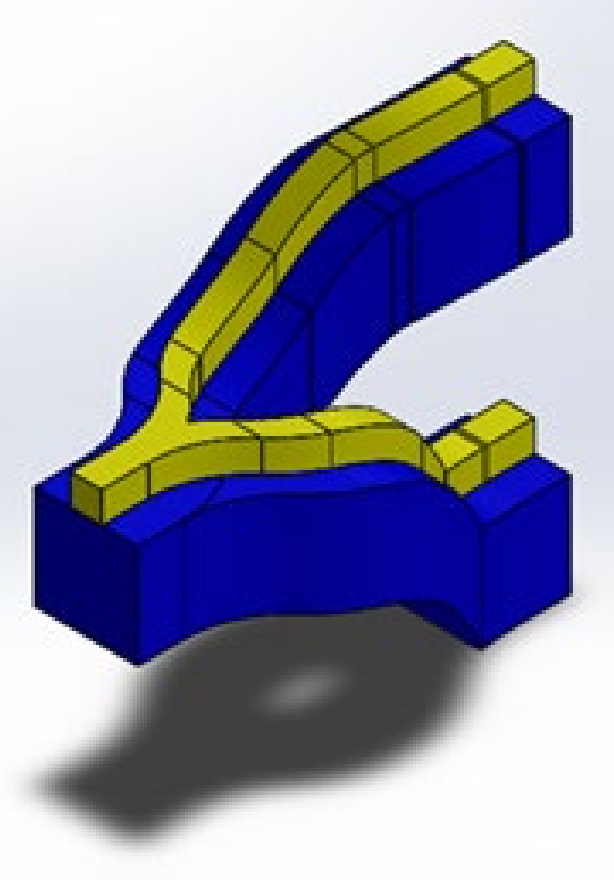

Figure 25. 3-D "Y" Merge in Multidimensional Channel Array.

For channel cross-sections with electrodes on opposing sides of the bacterial slurry channel, such as Figure 6 (C), the yellow electrode segments portrayed in Figure 25 would be mirrored on the underside of the channels as well as along the top and could be combined in a subsequent application of the 3-D "Y" merger to yield a single electrode segment. Incorporating this "Y" merger into this research's demonstrated "T" based channels is a potential avenue for future experimentation and analyses.

THIS PAGE INTENTIONALLY LEFT BLANK

IV. DISCUSSION

This section discusses the results obtained through this research to include sources of error and uncertainty. This chapter also provides some suggestions for potential applications and future research opportunities.

A. 3-D PRINTING FOR FABRICATION OF SQUARE AND "T" BASED CROSS-SECTION MICRO-INTERNAL STRUCTURES

The results presented in III.A and III.B show that 3-D PolyJet printing can achieve microscale internal channels featuring square and "T" based cross-section architectures. The 3-D printing manufacturing method allows for rapid creation of these micro-internal structures at a moderate cost with significantly less waste than subtractive manufacturing processes.

From the width measurement data versus clearance percentage for the square geometries it is determined that dimensions of approximately 1000-microns are reasonably well created and cleared with a high degree of predictability. Also, the consistency of creation and clearance decreases with decreasing dimensionality. The smallest channels cleared in this research measured at approximately 200-microns, and at these smaller dimensions, higher levels of uncertainty in clearance percentage were observed.

From the percentage clearance data associated with both the square and "T" based geometries it is clear that there are sources of error and uncertainty present in the manufacturing processes used in this research. One source of error comes from the nature of the printing process. The process used by the printer is to deposit liquid resin which spreads briefly and is then cured by UV light. This spreading yielded irregular and ambiguous edges in the channels.

The data also shows that the fidelity of created dimensions compared to the planned dimensions decreases as the planned dimensionalities decrease. It is important to note that although many of the channels created and cleared presented dimensions greater than what was planned, the results, particularly for the larger dimensions, were largely in keeping with the printer's uncertainty tolerances. This leads to two areas of future research and

optimization. One opportunity for research is to determine if the repeatability of the channels can be improved. Another research avenue could investigate if smaller dimensions can be achieved by manipulation of the CAD drawings, improved print area grid alignment, or print mode variation. Additionally, the lower dimensions achievable by this manufacturing method provide critical data that can be used in future electron capture optimization and scalability analysis.

The two-dimensional nature of the images used to analyze and compare the three-dimensional reference and sample channels contributed another source of uncertainty as shadowing effects made it difficult to fully discern the extent of imperfections within the channels. The clearing processes involves exposing the sacrificial material to sodium hydroxide to chemically break the material down for removal from the channels. This chemical etching may also introduce irregularities in the sacrificial material that is not fully removed from the channels. The edge irregularities and ambiguities were particularly prevalent in the reference samples. These discrepancies introduced uncertainties throughout the tracing of the channels which propagated uncertainties throughout the subsequent numerical analyses.

There is also potential for optical lensing effects to be present due to variations of the index of refraction when viewing the channels under a microscope, this could be confirmed and better analyzed through reducing the structural depth of the chips. These effects, if present at all, are not believed to have played a significant result in the measurements obtained in this research. Improvement and repetition of the chip clearing procedures developed in this research could lead to improved micro-channel clearance percentages.

The post-printing procedure developed during this research for removing the sacrificial material yielded promising results but requires notable manual action and time. Full post-print processing of a single chip took approximately 7–8 hours with most of the variation coming from the time invested in the manual flushing of the channels, step 7 of the micro-channel clearing procedures presented in Table 1. Print times were reasonably quick, taking 1–3 hours depending on the number of chips being printed during the run. For this research, batches of three to four chips were printed during a single print run.

Combining the print time marks and post-processing time marks yields the entire fabrication process time for a small batch of chips to be 8–11 hours. The output volume for completed chips versus time invested could be optimized by fully utilizing the print volume available in the printer and refining or automating the post-print processing procedures. Improving the output volume per unit of time will be beneficial as this technology matures into a production and employment stage of its life cycle.

B. SELF-ASSEMBLED WIRING

The results presented in III.C demonstrate proof of concept that the "T" based cross-section architecture is capable of supporting microfluidic separation by entrapping a hydrophobic material within the "T" flanges while water replaces the material within the bacterial slurry channel. This effect can support self-assembly of internal wiring to support various micro-technologies including BMFCs. There are a variety of factors that affect these results and there are many areas of improvement that offer future research opportunities.

Since the self-assembly of internal wiring in this application is based on surface tension and fluid separation, the viscosity of the oil was an important factor in achieving this effect. For this experiment, the dyed oil needed to have a low enough viscosity to be easily passed through a 1cc syringe with luer tip. Since the oil paint comes in a dense paste form, it needed to be thinned down. Thinning the oil-paint was accomplished by beginning with a small amount of paint, ~0.85g, added to a centrifuge tube and then vegetable oil was added in 1cc intervals and mixed via a Scientific Industries Vortex-Genie 2. After mixing, attempts to fill and discharge the solution through the syringe and luer tube were made. This process was repeated until the solution easily passed through the syringe with the luer tip. The finalized solution was ~0.85g of the paint and ~4.61 grams of vegetable oil which yields a ratio of approximately 5.42:1. The viscosity of the material to be used as electrodes in the device is a parameter that can be optimized to improve the self-assembled wiring effect. The material must be viscous enough to remain in the channels during flushing but not so viscous that it cannot be introduced into the channels. The material used for the

electrodes must also not harm the bacteria that will reside within the bacterial slurry channel.

The clearance of the sacrificial material within the channels is another aspect that had important effects on these experiments. Since the channels were not perfectly created and cleared, there may have been obstructions and edge irregularities that could have caused flow within the channels to become inconsistent and turbulent. This turbulence could be significant enough to have forced the oil out of the flanged sections and into the bacterial slurry channel during rinsing, ultimately yielding a failed result for self-assembly of internal wiring. By improving the post-printing clearing procedures or by repeating the procedures, the clearance within the channels could be improved and more consistent results may be achieved.

The pressure applied during loading the chips with the oil and rinsing with water also had an impact on the success of the self-assembled wiring effect. These experiments were carried out by manual loading of the substances into the channels using 1cc syringes with luer tips. The pressure necessary to load and rinse the channels varied slightly as determined by feel. This is likely due to the geometric variations and imperfections in channel clearances. Generally, the smaller channels required slightly more pressure to load and rinse than the larger geometries. Also, the pressure required to rinse the channels felt generally higher than the pressure needed to initially load the channels with oil. This effect is as expected due to the higher resistance of the oil to vacate the channel when acted on by the water compared to the resistance of air vacating the channels when being filled with the oil. The pressures used in these experiments needed to be high enough to fill and flush the channels but not so strong that the flow regimes became turbulent and forced the oil to vacate the flanges. This process could be improved by optimizing and better controlling the pressure applied during channel loading and rinsing. The pressure could be controlled by incorporating an air-compressor with regulators to standardize the applied pressures. Additionally, optimizing the inlet and outlet port designs may also improve channel loading and flushing.

The self-assembly of wiring results can be combined with the architectural configuration presented in Figure 25 to permit multiple channels to be combined into a

single continuous channel. This could simplify the design to combine multiple channels with single inlet and outlet ports. This would enable the design to be scaled up to yield higher power densities per device and may be capable of being printed as a single piece.

C. FUTURE WORK

A critical element to the progression of this technology is the development of a conductive material to make up the electrodes in support of the self-assembled wiring. The material that makes up the self-assembled wiring must be capable of capturing electrons generated within the bacterial slurry and transporting the captured electrons to a load. The wiring material must be capable of conducting electricity as well as not harming the bacteria residing in the channel.

One possible avenue for achieving the desired electrical characteristics is to infuse a biocompatible oil or resin with conductive nanoparticles. Regarding the electrical characteristics, one metric used to characterize the effectiveness of a material at transporting electrons is the material's conductivity. One method of determining conductivity is by first measuring the material's resistance, R, and using this parameter to calculate the resistivity, ρ, and ultimately the conductivity, σ. The resistance can be calculated by dividing the measured voltage, V, by the applied current, I, as shown by Equation (4.1). From the known dimensions of the sample, the resistivity, ρ, can be calculated by Equation (4.2) and then the conductivity, σ, from Equation (4.3).

$$R = \frac{V}{I} \tag{4.1}$$

$$\rho = \frac{RA}{L} \tag{4.2}$$

$$\sigma = 1/\rho \tag{4.3}$$

The materials being investigated for the desired electrical properties could be simultaneously investigated for compatibility with potential strains of bacteria that are intended to reside within the BMFC.

Once a suitable material is developed for use as the wiring, the next logical step in experimentation will be to load the chip configurations developed in this research with the wiring material and a bacterial slurry and obtain power output measurements. These measurements can be used to make determinations on architectural optimizations and can be compared to the results obtained in the 2019 NPS research to determine further directions for investigation and experimentation.

Another avenue for further research, complimentary to the presented conductivity and biocompatibility avenue, is to simplify the manufacturing process by leveraging hybrid printing of the "T" flange internal structures. The printer used in this research does not currently pose a commercially available print material with the desired characteristics. A material capable of being PolyJet 3-D printed along with posing the desired biocompatibility and electrical properties could greatly simplify the manufacturing process and enable quicker fabrication of a scaled up BMFC device.

One approach to creating this type of material is to spike a printable resin with conductive nanoparticles. Developing a printable resin with conductive and biocompatibility properties is another area for future research. Even with the proper electrode material and hybrid printing, the post-print processing would not be completely eliminated, but it would be simplified to clearing a square cross-section channel instead of the more complicated "T" based architectures. This advancement would eliminate the need for dual fluid filling and flushing of the device. If printed and cleared successfully, the device would ultimately only need to be loaded with the bacterial slurry and connected to the desired load.

V. CONCLUSION

This research has demonstrated that hollow internal structures can be PolyJet 3-D printed and cleared at the micro-scale. Square cross-section channels were successfully created featuring widths ranging between approximately 200-microns to 1000-microns. "T" based cross-sectional architectures were also successfully printed and cleared to similar dimensions. These "T" based sample channels were used to demonstrate proof of concept for a 3-D printable architecture capable of achieving self-assembled internal wiring to support BMFC technology.

These results are promising for advancing BMFC technologies in terms of economical production and scalability of output power through device geometry upscaling. Combining the "T" based self-assembled wiring concept with the 3-D "Y" merger architecture concept yields a pathway to a fuel cell architecture capable of being 3-D printed as a single piece with single inlet and outlet ports. This research's application and many others require a fluidic material with electrically conductive and biocompatible characteristics. Ideally, this material would also be capable of being 3-D printed in a hybrid mode alongside non-conductive resins in the same device, at high resolution and at multiple levels within the device. This material and capability combination is not yet commercially available and is a critical subject for future related research efforts.

This research supports the Navy's climate action efforts by advancing technology capable of supporting a scalable BMFC. A scaled up BMFC could be used to support moderate energy needs of military vehicles and equipment distributed across the maritime environment without leveraging fossil fuels. Future military applications and employment strategies for this technology offer a wide avenue for future research.

This research may also provide insight for a many commercial applications. The results presented may benefit a range of biomedical device technologies by providing insight into the capabilities and limitations posed by PolyJet 3-D printing of square and "T" based cross-section hollow internal structures at relevant scales. Commercial maritime

applications for distributed networks of BMFC based energy stations is another avenue yet to be explored but may be well suited for charging at anchorages.

Success in attaining energy sustainability will hinge on the ability to harness energy from a variety of sources that are locally available and naturally replenishable. This research supports the U.S. Navy's initiatives by providing advancements to technologies that provide renewable energy sources needed to sustain manned and unmanned systems operating in remote regions.

LIST OF REFERENCES

[1] "Department of the Navy Climate Action 2030 220531.pdf." Department of the Navy, Office of the Assistant Secretary of the Navy for Energy, Installations, and Environment, May 2022. Accessed: Jul. 12, 2022. [Online]. Available: https://www.navy.mil/Portals/1/Documents/Department%20of%20the%20Navy%20Climate%20Action%202030%20220531.pdf?ver=3Q7ynB4Z0qUzlFg_2uKnYw%3d%3d&timestamp=1654016322287

[2] D. Londoño-Pulgarin, G. Cardona-Montoya, J. C. Restrepo, and F. Muñoz-Leiva, "Fossil or bioenergy? Global fuel market trends," *Renew. Sustain. Energy Rev.*, vol. 143, p. 110905, Jun. 2021, doi: 10.1016/j.rser.2021.110905.

[3] B. E. Logan, *Microbial Fuel Cells*. Hoboken, UNITED STATES: John Wiley & Sons, Incorporated, 2008. Accessed: Jul. 12, 2022. [Online]. Available: http://ebookcentral.proquest.com/lib/ebook-nps/detail.action?docID=331621

[4] "CNO NAVPLAN 2021 - FINAL.pdf." Accessed: Jul. 12, 2022. [Online]. Available: https://media.defense.gov/2021/Jan/11/2002562551/-1/-1/0/CNO%20NAVPLAN%202021%20-%20FINAL.PDF/CNO%20NAVPLAN%202021%20-%20FINAL.PDF

[5] "PB23 SHIPBUILDING PLAN 18 APR 2022 FINAL.pdf." Office of the Chief of Naval Operations Deputy Chief of Naval Operations for Warfighting Requirements and Capabilities - OPNAV N9 2000 Navy Pentagon Washington, DC, 20350-2000, Apr. 2022. Accessed: Jul. 12, 2022. [Online]. Available: https://media.defense.gov/2022/Apr/20/2002980535/-1/-1/0/PB23%20SHIPBUILDING%20PLAN%2018%20APR%202022%20FINAL.PDF

[6] M. Gilday, "NAVIGATION PLAN 2022_SIGNED.pdf." Chief of Naval Operations, 26JUL2022. Accessed: Jul. 29, 2022. [Online]. Available: https://media.defense.gov/2022/Jul/26/2003042389/-1/-1/1/NAVIGATION%20PLAN%202022_SIGNED.PDF

[7] Y. Gong, S. E. Radachowsky, M. Wolf, M. E. Nielsen, P. R. Girguis, and C. E. Reimers, "Benthic Microbial Fuel Cell as Direct Power Source for an Acoustic Modem and Seawater Oxygen/Temperature Sensor System," *Environ. Sci. Technol.*, vol. 45, no. 11, pp. 5047–5053, Jun. 2011, doi: 10.1021/es104383q.

[8] L. Shelby, "THE SMALL, THE AGILE, AND THE MANY: REIMAGINED NAVAL POWER," *Nav. Sci. Technol.*, vol. 8, no. 1, p. 40, 2022, Accessed: Jul. 15, 2022. [Online]. Available: https://www.nre.navy.mil/media/document/future-force-vol-8-no-1-2022

[9] T. D. Nguyen, “OUTPUT POWER OPTIMIZATION OF MICROBIAL FUEL CELLS BY SCALABLE MICROFLUIDIC DEVICES,” Monterey, CA; Naval Postgraduate School, 2019.

INITIAL DISTRIBUTION LIST

1. Defense Technical Information Center
   Ft. Belvoir, Virginia

2. Dudley Knox Library
   Naval Postgraduate School
   Monterey, California

DUDLEY KNOX LIBRARY

NAVAL POSTGRADUATE SCHOOL

WWW.NPS.EDU

WHERE SCIENCE MEETS THE ART OF WARFARE